

Strong Second- and Third-Harmonic Generation in 1D Chiral Hybrid Bismuth Halides

Li Yao,* Zhouxiaosong Zeng, Chengkun Cai, Peng Xu, Honggang Gu, Liang Gao, Junbo Han, Xiaowei Zhang, Xi Wang, Xiao Wang, Anlian Pan, Jian Wang,* Wenxi Liang, Shiyuan Liu, Chao Chen, and Jiang Tang

Cite This: *J. Am. Chem. Soc.* 2021, 143, 16095–16104

Read Online

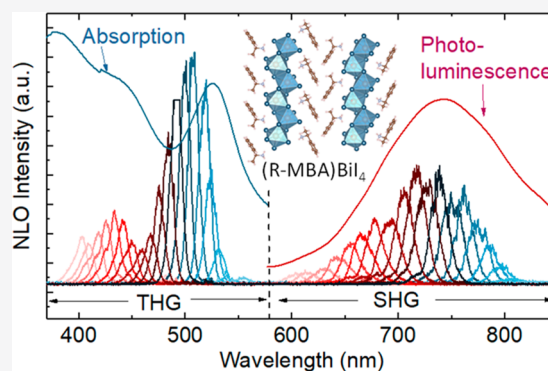
ACCESS |

Metrics & More

Article Recommendations

Supporting Information

ABSTRACT: Breaking the symmetry of a crystal structure can enable even-order nonlinear activities, including second-harmonic generation (SHG). The emerging chiral hybrid organic–inorganic metal halides feature unique optical and electronic properties and flexible crystal structures, making them a class of promising nonlinear optical materials. However, their nonlinear response performances are currently inferior to traditional nonlinear crystals, because of the lack of research on resonant enhancement and third-harmonic generation (THG). Herein, we designed chiral hybrid bismuth halides with naturally nonsymmetrical structure to enable SHG. Simultaneously, these chiral compounds preserve 1D crystal structures to create strong free exciton, broad self-trapped exciton (STE), and discrete band energy levels, which facilitate the resonant enhancement of SHG and THG susceptibilities. These new chiral films showcase superior effective SHG susceptibility ($\chi^{(2)} \sim 130.5 \text{ pm V}^{-1}$ at an interesting wavelength of 1550 nm), exceeding that of the reference, a commercial LiNbO_3 ($\chi^{(2)} \sim 83.4 \text{ pm V}^{-1}$) single-crystal film. Furthermore, their THG intensities are even higher than their SHG intensities, with effective THG susceptibility ($\chi^{(3)}$) being $\sim 9.0 \times 10^6 \text{ pm}^2 \text{ V}^{-2}$ at 1550 nm (37 times that of the reference monolayer WS_2). Their high SHG and THG performances indicate the promising future of these 1D chiral hybrid bismuth halides toward nonlinear optical applications.



lithium niobate (LiNbO_3),⁸ KTiO_2PO_4 (KTP),⁹ KH_2PO_4 (KDP),⁹ and $\beta\text{-BaB}_2\text{O}_4$ (BBO),⁹ dominate the commercial NLO markets because of their relatively high SHG susceptibility, high pure crystal form, high mechanical strength, and good physicochemical stability.¹⁰ However, with the increasing demand for flexible, miniaturized, and integrated NLO devices, the incompatible preparation and difficulty in modification of the inorganic NLO materials become increasingly prominent issue, so the development of novel NLO materials is essential for the advancement of NLO field. The emerging hybrid organic–inorganic perovskites^{11–13} feature flexible crystal structures, a low-temperature and scalable solution fabrication process, and tunable optoelectrical properties, showing great potential as a new class of NLO material.

INTRODUCTION

Nonlinear optics is a field of study concerned with interactions between intense laser light beams and materials. Second-harmonic generation (SHG) and third-harmonic generation (THG) are important branches of nonlinear optics.¹ Until the invention of the laser,² Franken and his colleagues first demonstrated the SHG process in quartz by using a pulsed ruby laser in 1961,³ opening up a whole new era of nonlinear optics. SHG (THG) are nonlinear processes of converting two (three) low-frequency photons into one coherent high-frequency photon within a nonlinear medium. Such frequency-doubling or frequency-tripling processes are the key basis of laser manufacturing,⁴ optical communication,⁵ therapy,⁶ and military applications.⁷

SHG can only be generated in noncentrosymmetric materials or interfaces. For centrosymmetric medium, during the second-order nonlinear optical (NLO) process (that is, $\mathbf{P} = \epsilon_0 \chi^{(2)} \mathbf{E}^2$), the induced second-order polarization \mathbf{P} must change sign as the sign of the applied electric field \mathbf{E} changes, leading to the complete vanishing of SHG susceptibility ($\chi^{(2)}$). In contrast, there are no such structural restrictions on THG materials. Thus, a possible nonzero THG susceptibility ($\chi^{(3)}$) exists in all materials. Currently, inorganic NLO materials, e.g.,

Received: June 24, 2021

Published: September 24, 2021

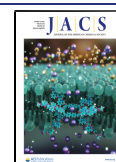


Table 1. Effective SHG ($\chi^{(2)}$) and THG Susceptibilities ($\chi^{(3)}$) of Various Chiral Hybrid Organic–Inorganic Metal Halides^a

chiral hybrid metal halides	form	dimensionality	$\chi^{(2)}$	$\chi^{(3)}$	λ_{pump}	ref
(<i>R</i> -MPEA) _{1.5} PbBr _{3.5} (DMSO) _{0.5}	nanowire	2D	0.68		850	14
(<i>R</i> -MBA) ₂ CuCl ₄	film	2D	57.5		800	15
((<i>R</i>)-C ₈ H ₁₂ N) ₄ Bi ₂ Br ₁₀	powder	0D	SHG active		1064	16
[(<i>R</i>)-1-(4-F)PEA] ₄ Sb ₂ Cl ₁₀	crystal	0D	SHG active		800	17
(<i>R</i> -MBA)BiI ₄	film	1D	130.5	9.0 × 10 ⁶	1550	this work

^aThe units of pump wavelength (λ_{pump}), $\chi^{(2)}$, and $\chi^{(3)}$ are nm, pm V⁻¹, and pm² V⁻², respectively. PEA = phenethylammonium; MA = methylammonium; MPEA = methylphenethylammonium; MBA = methylbenzylammonium.

Nevertheless, the high structural symmetry of perovskites¹⁸ makes them immune to SHG. For example, Frohna et al. confirmed no SHG signal from the bulk of tetragonal CH₃NH₃PbI₃ with a *D*_{4h} point group.¹⁹ Thus, the next step to get SHG is to break the centrosymmetry of the perovskite crystal structure. The effective way to change their crystal structure is to incorporate distinct organic molecules. Generally, a chiral organic molecule contains more than four atoms or functional groups arranged around a C atom with neither symmetric center nor symmetric plane. After the insertion of enantiopure chiral organic molecules into a perovskite framework, the resulting compounds obtain a chiral crystal structure (noncentrosymmetric) through the chirality transfer from the organic to the inorganic part.²⁰ Simultaneously, their crystal structure also deviates from the standard perovskite structure, and thus these chiral compounds should not continue to be classified as perovskites but as hybrid organic–inorganic metal halides.^{21,22} Recently, new chiral hybrid metal halides shine in the fields of circularly polarized photoluminescence,²³ ferroelectrics,²⁴ circularly polarized light photodetectors,^{25,26} spintronic applications,²⁷ and NLO.^{14–17} Their exploration in the NLO field is still in its infancy (Table 1). Compared to the conventional nonlinear material (such as LiNbO₃, $\chi^{(2)} \sim 83.4$ pm V⁻¹),²⁸ their effective conversion wavelength range, stability, and NLO susceptibilities still need to be improved.

The approach to improve the SHG and THG performance of chiral hybrid metal halides is to create effective exciton transition level as a basis for resonant enhancement. The harmonic generation process involves one occupied state and two (for SHG) or three (for THG) virtual transition states.¹ When the upmost virtual transition levels of SHG and THG are nearly coincident with one excited state energy level of the material, a resonance enhancement of the NLO susceptibility will occur.¹ Wang et al.²⁹ previously found that the SHG efficiency in WSe₂ monolayer could be enhanced by 3 orders of magnitude at the exciton resonance energies in 4K. For chiral hybrid metal halides, the large cation radii of chiral organic molecule render it devoid of connectivity between the metal–halide octahedra, thus lowering its structural dimensionality. On the other hand, heterovalent ion substitutions, such as Pb²⁺ replaced by Bi³⁺ or Sb³⁺, can also promote the formation of a lower-dimensional structure to maintain the charge neutrality.³⁰ Such a low-dimensional structure and a soft lattice give rise to strong electron–phonon coupling, which is essential for the formation of a self-trapped exciton (STE). Furthermore, the low-dimensional structure brings a large free exciton (FE) binding energy, and the discrete band transition states resemble 0D quantum dots. These various excitonic energy levels enable the possible realization of the resonant enhancement of SHG and THG.^{31,32}

In this work, we designed chiral hybrid organic–inorganic bismuth halides with efficient SHG and THG performance. These compounds have a one-dimensional (1D) chiral crystal structure. Their symmetry-breaking structure makes them capable of SHG. Their 1D structures offer strong FE, STE, and discrete band energy levels for resonant enhancement of SHG and THG with a broad resonance wavelength range (400–800 nm). The SHG susceptibility of this chiral hybrid bismuth halide film at a pump wavelength of 1550 nm surpasses that of the reference, a LiNbO₃ single-crystal film. The first discovery of strong THG signals in chiral hybrid metal halides enable its potential applications in ultraviolet coherent light generation.

■ RESULT AND DISCUSSION

Symmetry-Breaking Structure. The symmetry-breaking structure of a material is a prerequisite for SHG. Therefore, we first investigate the crystal structure of the chiral hybrid bismuth halides. (*R*- and *S*-MBA)BiI₄ single crystals (elongated orthorhombic red crystals, Figure S1a) were grown by a temperature-lowering crystallization process. Briefly, an aqueous HI solution containing stoichiometric amounts of *R*- (+)- or *S*-(-)- α -methylbenzylammonium (*R*- or *S*-MBA) and Bi₂O₃ was used as the growing mother liquid. (*R*- and *S*-MBA)BiI₄ crystallize in orthorhombic *P*2₁2₁ space group (see Table S1 for crystallographic data), which belongs to the Sohncke type, indicating that (*R*- and *S*-MBA)BiI₄ have chiral crystal structures.²⁰ The powder X-ray diffraction (XRD) patterns of (*R*- and *S*-MBA)BiI₄ powder are well in line with the corresponding simulated results from crystal structure, which proves the single-phase (Figure S1b). The crystal structures of (*R*- and *S*-MBA)BiI₄ are presented in Figure 1a and 1b, respectively. (*R*- and *S*-MBA)BiI₄ are composed of helical [BiI₄]⁻ chains (edge-sharing BiI₆ octahedra), which are embraced by chiral MBA⁺ cations and extend parallel to the *a*-axis. These two chiral compounds can be classified as 1D structures based on the effective dimensionality of their inorganic framework. These two enantiomers exhibit opposite helicities and are a mirror image of each other. The -NH₃⁺ “head” of the chiral MBA⁺ cation points toward the vicinity of two adjacent octahedra. The chirality transfers induced by the NH₂-H...I-Bi hydrogen bond interactions result in the asymmetric tilts and distortions of BiI₆ octahedra (as indicated in Figure 1c,d). The significant tilts and distortions give rise to two unique Bi atoms with a Bi-I-Bi bond angle largely deviating from 180° (~171°) and Bi-I bond lengths changing from 2.91 to 3.30 Å (Tables S2 and S3). The calculated distortion levels of two [BiI₆]³⁻ octahedra are 1.5 × 10⁻³ and 2.3 × 10⁻³, respectively, which are an order of magnitude higher than those of (*R*-MPEA)₂CuCl₄ and (*S*-MPEA)₂CuCl₄.³³ Notably, relative to the chiral MBA⁺ cations on one side of the inorganic chain, the cations on the other

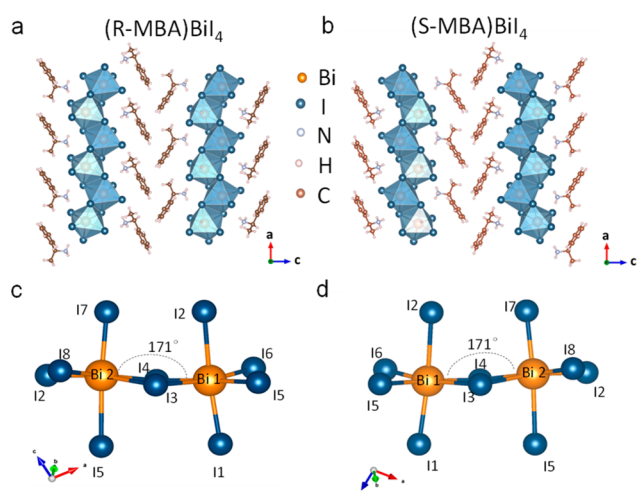


Figure 1. Crystal structures of chiral hybrid bismuth halides. Crystal structures of (a) $(R\text{-MBA})\text{BiI}_4$ and (b) $(S\text{-MBA})\text{BiI}_4$ projected along the b -axis. The $[\text{Bi}_2\text{I}_8]^{2-}$ building block composed of two edge-connected octahedra from (c) $(R\text{-MBA})\text{BiI}_4$ and (d) $(S\text{-MBA})\text{BiI}_4$.

side twist the $-\text{NH}_3^+$ “head” by 56° (Figure S2), which enhances the asymmetry of the chiral structure.

Unique Electronic Structures. SHG and THG are highly sensitive to the materials’ electronic structures, especially exciton states. The calculated band structures of $(R\text{-MBA})\text{BiI}_4$ (Figure 2a) show discrete energy level distributions in the conduction band (CB, noted as CB1, CB2, and CB3 by different colors). The band structure is calculated by the Perdew–Burke–Ernzerhof functional³⁴ with the spin–orbit coupling effect considered. Figure 2b shows the linear absorption and corresponding circular dichroism (CD) spectra of these chiral films. Thin films of $(R\text{-}$ and $S\text{-MBA})\text{BiI}_4$ were obtained by the one-step spin-coating method. The absorption spectra show a sharp resonance centered at ~ 525 nm, and four relatively broadband transitions centered at ~ 446 , ~ 380 , ~ 317 , and ~ 265 nm. This feature of multiple absorption peaks commonly exists in other 1D bismuth-based hybrid metal halides.³⁵ The sharp absorption was designated as an FE transition, and other broad absorptions were designated as valence band (VB) to CB transitions.³⁵ Corresponding to nearly each absorption peak wavelength, the CD spectra of $(R\text{-}$ and $S\text{-MBA})\text{BiI}_4$ films (Figure 2b) cross the zero line. Such a CD signature is known as the bisignate Cotton effect. Each bisignate signal may be related to the splitting of the energy level of inorganic part under the influence of chiral organic ligand into two new sublevels, which are preferentially excited

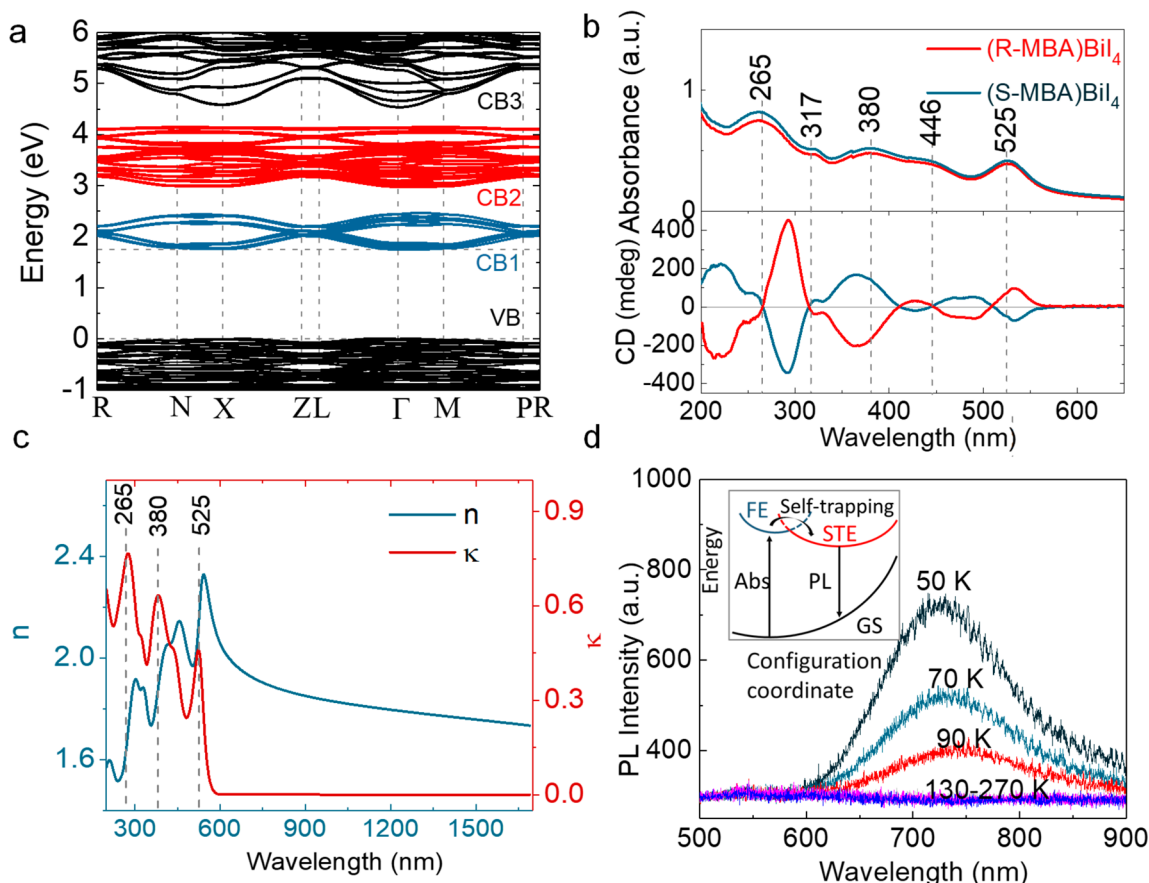


Figure 2. Unique electronic structures in 1D chiral hybrid bismuth halides. (a) Calculated band structure of $(R\text{-MBA})\text{BiI}_4$. VB and CB indicate valence band and conduction band, respectively. (b) Absorption spectra and the corresponding circular dichroism (CD) spectra of $(R\text{-MBA})\text{BiI}_4$ (red line) and $(S\text{-MBA})\text{BiI}_4$ (blue line) films on quartz measured at room temperature. The CD signals relate to the differences in absorptions of the left-handed (A_L) versus right-handed (A_R) circularly polarized light by the equation: $\text{CD} [\text{mdeg}] = 32980 \times \Delta A$, here, $\Delta A = A_L - A_R$. (c) Refractive index (n) and extinction coefficient (κ) values of $(R\text{-MBA})\text{BiI}_4$ film obtained from ellipsometer measurement. (d) Temperature-dependent photoluminescence spectra of a single crystal of $(R\text{-MBA})\text{BiI}_4$ (excited at 365 nm). Inset: a schematic indicates the processes (arrows) of FE absorption (Abs), self-trapping, and the STE emission (PL), as well as the energy surfaces (curves) of ground state (GS), FE, and STE.

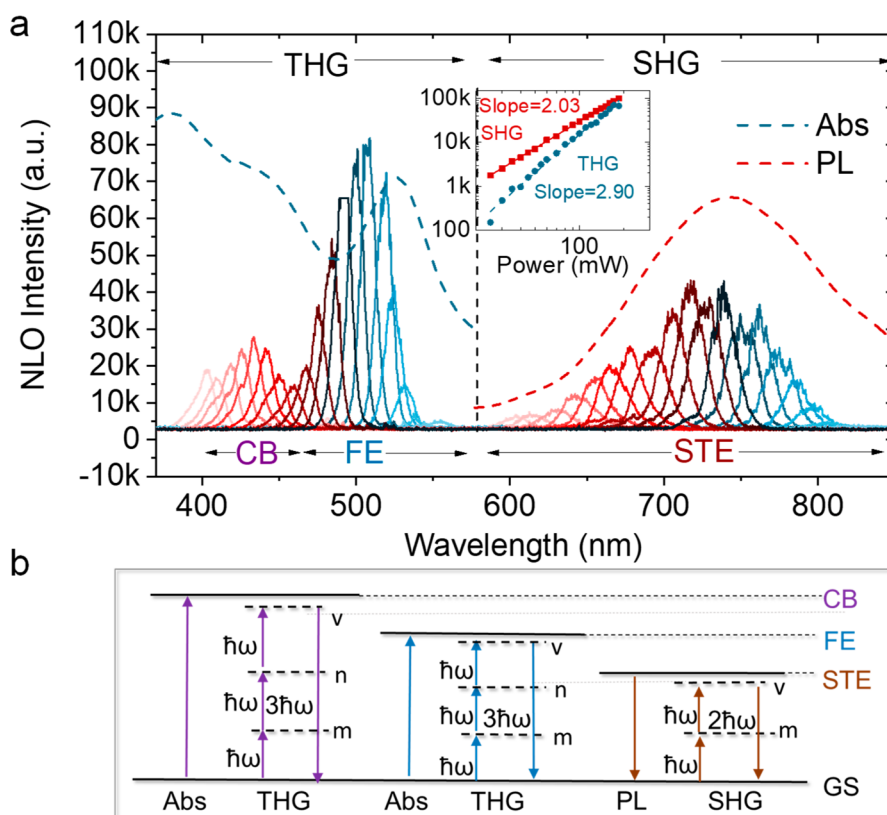


Figure 3. Wavelength-dependent SHG and THG response of (R-MBA)Bi₄. (a) Wavelength-dependence of SHG and THG intensities for (R-MBA)Bi₄ film at room temperature. The pump power is fixed at 100 mW. The pump wavelength extended from 1200 to 1650 nm with 25 nm intervals. The short-wavelength part belongs to THG, and the long-wavelength part belongs to SHG, separated by a vertical dotted line for clarity. The rescaled PL spectrum at 90K (red dash line, right) and absorption (Abs) spectrum (blue dash line, left) of (R-MBA)Bi₄ are shown for reference to the envelopes of the set of SHG and THG spectra, respectively. Inset: power-dependence of SHG and THG intensities for (R-MBA)Bi₄ film at $\lambda_{\text{pump}} = 1275$ nm, plotted on a log–log scale with power-law fits. (b) Schematic for excited state resonant SHG or THG processes. The upper virtual transition energy levels (v) are nearly coincident with the CB, FE, and STE levels, respectively. The band-edge VB to CB absorption (Abs), FE absorption (Abs), and STE emission (PL) processes are resonant with THG, THG and SHG processes, respectively. The virtual transition levels are denoted as v , n , and m .

by the opposite circular polarization.^{25,36} Here, five bisignate CD signals and absorption peaks demonstrate the existence of five transition energy levels or bands, while in previously reported chiral perovskites or chiral hybrid metal halides, only one or two bisignate signals can be observed.^{37,38} Furthermore, the effective refractive index n and extinction coefficient κ (Figure 2c and Table S4) of (R-MBA)Bi₄ film were also measured by a spectroscopic ellipsometer. The dispersion relation of n relates to the phase mismatch on SHG and THG, as discussed later. The κ spectrum shows five evident peaks as the absorption spectra. Overall, (R- and S-MBA)Bi₄ were shown to possess the strong free excitonic state and discrete VB to CB transition states.

Through the temperature-dependent photoluminescence (PL) spectra (Figure 2d), we also discovered the STE state in (R-MBA)Bi₄. The (R-MBA)Bi₄ single crystal shows no PL signal at room temperature. At 90 K, a faint red emission appears in the range of 650–900 nm, which is incrementally blue-shifted with the further decrease in temperature. Such broad-band emissions with large Stokes shift are widely existed in ternary metal halides such as 1D CsCu₂X₃ (X = Cl, Br, and I),³⁹ A₃M₂I₉ (A = Cs and Rb; M = Bi and Sb),⁴⁰ hybrid metal halides such as 2D PEA₂MA_{*n*-1}Pb_{*n*}I_{3*n*+1},⁴¹ and perovskites of low electronic dimensionality such as Cs₂(Ag_{0.60}Na_{0.40})InCl₆.⁴² These works demonstrated the excited-state transient struc-

tural distortion by density functional theory calculations and the dynamic process of the formation of STEs by transient absorption/reflection spectroscopy analysis.^{41,42} As shown in the inset of Figure 2d, after photoexcitation, there are three possible transient processes involving STEs: the formation of a STE state through structural distortion, the self-trapping of electron and hole in the STE state through the exciton–phonon interaction, and the STE emission.

Wavelength-Dependent SHG and THG. The multiple exciton states and discrete VB to CB transition states provide suitable energy levels for the resonant enhancement of SHG and THG.^{1,31,43} To investigate the resonant enhancement, we studied the NLO responses of our chiral compounds excited at a series of pump wavelengths. The nonlinear emissions were collected in transmitted configuration by a home-built light path (details in Figure S3) equipped with a femtosecond pulsed laser (34.56 fs, 5 kHz). Since the NLO response of (R-MBA)Bi₄ and (S-MBA)Bi₄ have no difference under linearly polarized excitation, we only studied the NLO performance of (R-MBA)Bi₄. As shown in Figure 3a, under each pump wavelength, two clear response signals occur simultaneously. The central wavelengths of the low-frequency and high-frequency signals are one-half and one-third of the pump wavelength, respectively, corresponding to the expected SHG and THG signals. In addition, the SHG (THG) signals show

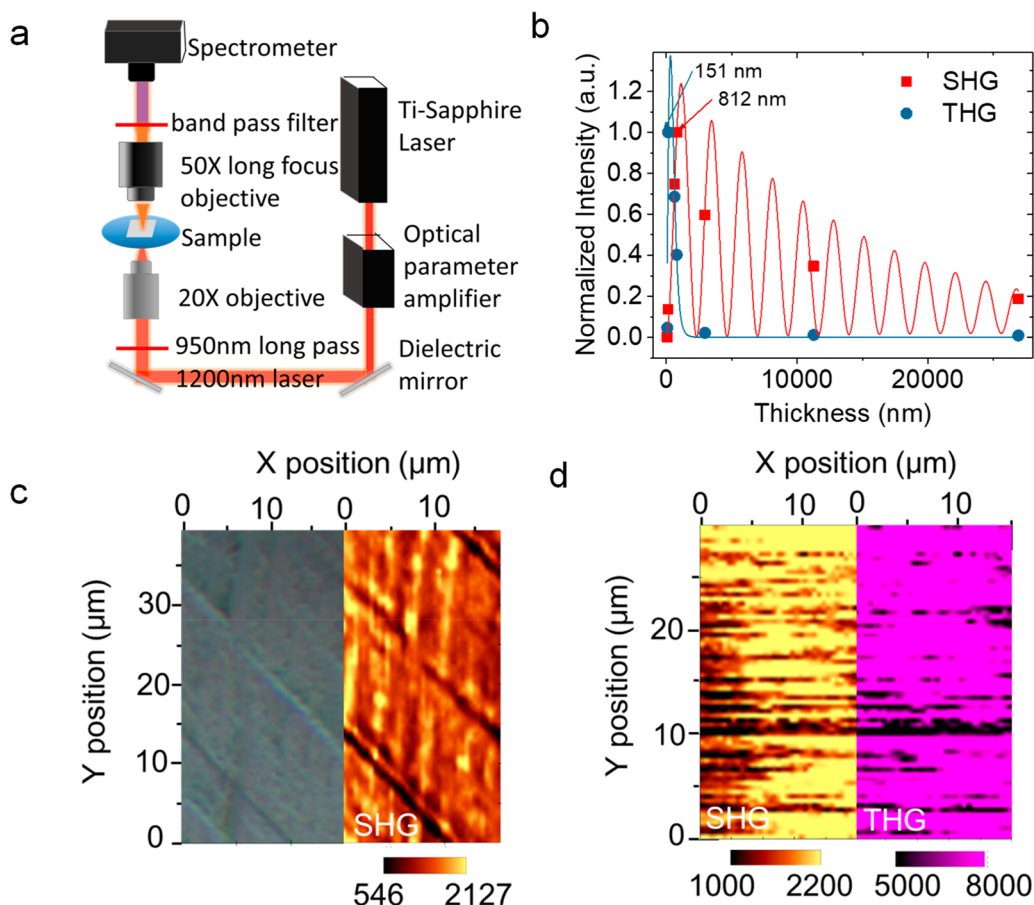


Figure 4. Thickness-dependent SHG and THG responses of (R-MBA)Bi₄. (a) The NLO microscopic measurement setup. The pump wavelength is fixed at 1200 nm. (b) Dependence of the SHG and THG signals with the film thicknesses for (R-MBA)Bi₄. The red and blue solid lines are the fits of the experimental data using eqs 3 and 4, respectively. (c) SHG mapping (centered at 600 nm) image and corresponding optical image of (R-MBA)Bi₄ film (~145 nm). (d) SHG mapping (centered at 600 nm) and THG mapping (centered at 400 nm) images of (R-MBA)Bi₄ film (~145 nm) for the same area under the same pump condition. The corresponding optical image is provided in Figure S4.

the quadratic (cubic) dependence of the SHG (THG) intensities with the pump power (inset of Figure 3a). The quadratic (cubic) dependence further demonstrates the energy conversion relationship of SHG (THG) process, that is, two (three) low energy photons convert into a high energy photon.¹ In summary, we carefully verified that the strong visible signals from (R-MBA)Bi₄ film were indeed caused by harmonic generation.

We choose the pump range of 1200–1650 nm to investigate the enhancement of SHG and THG. On the basis of this, the obtained SHG spectra could cover the broad STE emission wavelength range, while the obtained THG spectra fall within the absorption wavelength range. As shown in Figure 3a, we can see that the envelope of the sets of SHG spectra matches well with the spectral signature of the broad STE emission spectrum. Additionally, when the THG wavelength is close to the exciton absorption or band-edge absorption wavelength, the THG signal intensity is strongly enhanced. It should be noted that there is an energy deviation of ~83 meV between the strongest THG signal peak and the first exciton absorption peak. This deviation can be ascribed to a screened excitonic binding energy from exciton–exciton interaction in dense exciton gas, which was previously observed in 2D MAPbBr₃ nanosheets.⁴⁴ Eventually, the SHG is resonantly enhanced by ~24 times at STE energy; the THG is resonantly enhanced by ~47 times at the FE energy and by ~14 times at the band-edge

VB to CB transition energy. The resonantly enhanced THG emission at FE energy level had been proved in 2D (C₄H₉NH₃)₂(CH₃NH₃)Pb₂I₇ nanosheets despite with a narrow resonance wavelength range (~50 nm)³¹ and in 2D (CH₃(CH₂)₃NH₃)₂(CH₃NH₃)_{n-1}Pb_nI_{3n+1} [*n* = 1, 2, 3, and 4] at both the fundamental gap and the FE energy level.³² Here, the evident multiple exciton resonant enhancements of SHG and THG, especially SHG at the STE level, are demonstrated for the first time in chiral hybrid metal halides, which gives rise to a highly broad frequency conversion range covering almost the entire visible spectrum.

To better understand the nature of resonantly enhanced SHG and THG in (R-MBA)Bi₄, we provide a schematic (Figure 3b) combined with the expressions of SHG and THG susceptibility tensors ($\chi_{ijk}^{(2)}$ and $\chi_{ijkh}^{(3)}$) derived from time-dependent perturbation theory.^{1,29} The SHG and THG susceptibilities under the resonance case, i.e., one virtual transition state energy level of SHG and THG is close to one excited state energy level, are given in the following equations:²⁹

$$\chi_{ijk}^{(2)}(-2\omega; \omega, \omega) \propto \frac{\langle \psi_{gs} | \hat{V}_i^{2\omega} | \psi_{exc} \rangle}{E_{exc \rightarrow gs} - 2\omega h - i\Gamma_{exc \rightarrow gs}} \cdot \frac{\langle \psi_{exc} | \hat{V}_j^\omega | \psi_m \rangle \langle \psi_m | \hat{V}_k^\omega | \psi_{gs} \rangle}{E_{m \rightarrow gs} - \omega h - i\Gamma_{m \rightarrow gs}} \quad (1)$$

$$\chi_{ijkh}^{(3)}(-3\omega; \omega, \omega, \omega) \propto \frac{\langle \psi_{gs} | \hat{V}_i^{3\omega} | \psi_{exc} \rangle}{E_{exc \rightarrow gs} - 3\omega h - i\Gamma_{exc \rightarrow gs}} \cdot \frac{\langle \psi_{exc} | \hat{V}_j^\omega | \psi_m \rangle \langle \psi_m | \hat{V}_k^\omega | \psi_n \rangle \langle \psi_n | \hat{V}_h^\omega | \psi_{gs} \rangle}{(E_{n \rightarrow gs} - 2\omega h - i\Gamma_{n \rightarrow gs})(E_{m \rightarrow gs} - \omega h - i\Gamma_{m \rightarrow gs})} \quad (2)$$

where, $|\psi_{gs}\rangle$, $|\psi_{n,m,v}\rangle$, and $|\psi_{exc}\rangle$ denote the ground state, virtual intermediate states, and excited state, respectively. The excited state represents the CB, FE, or STE in Figure 3a,b. The vector \hat{V} is associated with the electric dipole, magnetic dipole, and electric quadrupole interactions.²⁹ $\Gamma_{exc \rightarrow gs}$ and $\Gamma_{n,m \rightarrow gs}$ denote the damping rate from the excited state and virtual states to the ground state, respectively. As the real excited state lives longer than virtual states, i.e., $\Gamma_{exc \rightarrow gs} \ll \Gamma_{n,m \rightarrow gs}$, the first term of eqs 1 and 2 is dominant.²⁹ When $E_{exc \rightarrow gs} \rightarrow 2\omega h$ or $E_{exc \rightarrow gs} \rightarrow 3\omega h$, that is, the NLO processes (SHG or THG) occur at the same energy as linear optical transitions (band-edge absorption, FE absorption, or STE emission), the nonlinear susceptibilities will increase sharply.¹

In general, the THG process is much weaker than the SHG process, because the former comes from a higher-order perturbation interaction in the polarization field.¹ However, as shown in Figure 3a, the THG signal of (R-MBA)BiI₄ is stronger than the SHG signal, and the THG/SHG intensity ratio reaches ~ 2 at a pump wavelength of 1500 nm. Säynätjoki et al.⁴⁵ reported a large THG/SHG intensity ratio (>30) in MoS₂. They explain this unusual phenomenon in MoS₂ by calculating the nonlinear response functions of 1L MoS₂ with emphasizing the role of trigonal warping.⁴⁵ The reason for the high THG/SHG intensity ratio in (R-MBA)BiI₄ is unclear. We think the further theoretical simulations of the SHG and THG susceptibilities may help to figure out the underlying physical mechanism.

Thickness-Dependent SHG and THG. The SHG and THG signals from a polycrystalline film may be influenced by film thickness, grain size, grain orientations, and film surface.¹⁹ To better illustrate this point, we used a microscopic detection system (Figure 4a) with a 1200 nm femtosecond pump laser (80 fs, 1k Hz) to measure the NLO response of our chiral film samples. For the study of the influence from film thickness, we measured the SHG and THG of a series of chiral films with the thickness extending from 80 nm to 27 μm (Figure 4b). The largest NLO signals occur for intermediate values, i.e., ~ 812 nm for SHG and ~ 151 nm for THG. Generally, analyzing Maxwell's nonlinear equation in specific conditions can essentially explain this thickness-dependent phenomenon.^{1,46} In our case ($\lambda_{\text{pump}} = 1200$ nm), the penetration depths (calculated as the reciprocal of absorption coefficient) of the SHG and THG signals are determined to be ~ 74 μm and ~ 55 nm, respectively. Moreover, the coherence lengths (calculated as the reciprocal of wavevector mismatch)¹ of the SHG and THG signals are determined to be about 364 and 298 nm,

respectively. Since the penetration depths and coherence lengths are less than our maximum film thickness, we considered both the NLO signal attenuation and phase mismatch in calculating Maxwell's nonlinear equation (see Supplementary Note 2). The dependence of SHG intensity (I_2) and THG intensity (I_3) with the film thickness (L) for our chiral film can be written as follows:

$$I_2(L) \propto (e^{-\alpha_2 L} - 2 e^{-\alpha_2 L/2} \cos(\Delta k^{(2)} L) + 1) e^{-\alpha_2 L} \quad (3)$$

$$I_3(L) \propto (e^{-\alpha_3 L} - 2 e^{-\alpha_3 L/2} \cos(\Delta k^{(3)} L) + 1) e^{-\alpha_3 L} \quad (4)$$

where α_n is the absorption coefficient of the n -fold frequency signal, and $\Delta k^{(n)}$ is the wavevector mismatch between the n -fold frequency wave with the pump wave. On the basis of eqs 3 and 4, the fits of the SHG and THG signals with film thicknesses of various thick film samples are provided in Figure 4b as solid lines. The resulting fitting values of α_n and $\Delta k^{(n)}$ have a good consistency with their experimental values (Table S5). For our different film samples, the influence from grain size and orientations on the NLO signals were similar (discussed in detail in Supplementary Note 1). Furthermore, the surface-induced SHG and THG signals were negligible, which was confirmed from the wavelength-dependent and thickness-dependent features of the NLO signals.

We also scanned the NLO signal of a certain thick (R-MBA)BiI₄ film. Comparing the SHG mapping with the corresponding optical image (Figure 4c), the SHG intensity change with the (R-MBA)BiI₄ film thickness fluctuation. For the optically uniform area (Figure S4) of the (R-MBA)BiI₄ film, the SHG and THG mapping images still present synchronous intensity changes (Figure 4d). Since the spectral resolution limit of our NLO measurement system (laser spot size ~ 3 μm) is much larger than the crystal grain sizes (30–50 nm, Figure S7a,b), the synchronous changes are unlikely to come from reduced SHG and THG intensity at grain boundaries. Therefore, we think the synchronous changes in Figure 4d may also come from the film fluctuations because the SHG and THG signals are highly sensitive to film thicknesses less than 150 nm (Figure 4b).

Quantification of SHG and THG Susceptibilities.

Effective SHG and THG susceptibilities are important figures of merit used to evaluate the performance of NLO materials. LiNbO₃ is a commercially employed NLO material, known for its high SHG susceptibility ($d_{33} = -41.7$ pm V⁻¹ at $\lambda_{\text{pump}} = 1058$ nm).²⁸ Transition metal dichalcogenides layered materials are widely investigated NLO materials with relatively high THG susceptibilities, like that of WS₂ (2.4×10^5 pm² V⁻² at $\lambda_{\text{pump}} = 1500$ nm).^{45,47,48} Then, we choose a purchased X-cut LiNbO₃ single-crystal film and a mechanically exploited monolayer WS₂ to quantitatively analyze the effective SHG and THG susceptibilities of our chiral (R-MBA)BiI₄ film. To ensure a similar confocal volume during SHG measurement, the LiNbO₃ film and our chiral film were chosen to have the same thickness. The detected SHG and THG intensities of these three samples are shown in Figure 5. Their effective SHG and THG susceptibilities ($\chi_{\text{eff}}^{(2)}$ and $\chi_{\text{eff}}^{(3)}$) are given and compared based on the following expressions (see Supplementary Note 3):

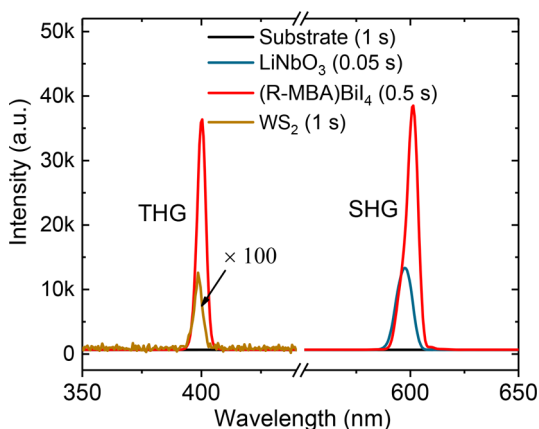


Figure 5. Quantification of SHG and THG susceptibilities of (R-MBA)Bi₄. Comparison of SHG and THG responses among ~600 nm (R-MBA)Bi₄ polycrystalline film, 600 nm X-cut LiNbO₃ single crystal film, and 0.7 nm monolayer WS₂. The pump power is 10 μW, and the pump wavelength is 1200 nm. The THG intensity of single-layer WS₂ is magnified by 100 times for clarity. The different integration times are labeled.

$$\chi_{\text{eff}}^{(2)} = \left[\frac{I_2(L)}{I_1(0)^2} \frac{8\epsilon_0 n_1^2 c^3 |\dot{n}_2|^2}{n_2 \omega_2^2} \frac{(\Delta k^{(2)})^2 + \alpha_2^2/4}{(e^{-\alpha_2 L} - 2e^{-\alpha_2 L/2} \cos(\Delta k^{(2)}L) + 1)} e^{\alpha_2 L} \right]^{1/2} \quad (5)$$

$$\chi_{\text{eff}}^{(3)} = \left[\frac{I_3(L)}{I_1(0)^3} \frac{16\epsilon_0^2 n_1^3 c^4 |\dot{n}_3|^2}{n_3 \omega_3^2} \frac{(\Delta k^{(3)})^2 + \alpha_3^2/4}{(e^{-\alpha_3 L} - 2e^{-\alpha_3 L/2} \cos(\Delta k^{(3)}L) + 1)} e^{\alpha_3 L} \right]^{1/2} \quad (6)$$

where \dot{n}_2 and \dot{n}_3 are the complex refractive indices at the second- and third-order harmonic wavelengths, respectively, n_1 is the refractive index at the fundamental wavelength, c and ϵ_0 are the vacuum light velocity and the vacuum permittivity, respectively, and the other parameters are the same as those in eqs 3 and 4. According to eqs 5 and 6, the $\chi_{\text{eff}}^{(2)}$ of (R-MBA)Bi₄ film was estimated to be ~39.4 pm V⁻¹, and its $\chi_{\text{eff}}^{(3)}$ was estimated to be ~8.5 × 10⁶ pm² V⁻². Furthermore, we also calculated the resonantly enhanced $\chi_{\text{eff}}^{(2)}$ and $\chi_{\text{eff}}^{(3)}$ of (R-MBA)Bi₄ film according to the wavelength dependence of SHG and THG in Figure 3a. The enhanced $\chi_{\text{eff}}^{(2)}$ and $\chi_{\text{eff}}^{(3)}$ at $\lambda_{\text{pump}} = 1550$ nm (an important communication wavelength) were estimated to be ~130.5 pm V⁻¹ (~1.6 times that of LiNbO₃) and ~9.0 × 10⁶ pm² V⁻² (~37.5 times that of WS₂), respectively. Compared with other chiral hybrid metal halides (Table 1), our material stands out for the simultaneous existence of SHG and THG with high susceptibilities. Due to the unique electronic structures, our chiral material can generate resonantly enhanced coherent lasers, covering frequencies from violet to near-infrared.

For future practical application, optical damage and longer-term environmental exposure of materials are important aspects to consider. We found that after exposure to the ambient environment for 3 months the powder XRD spectra of (R-MBA)Bi₄ showed no peak changes (Figure S6a), and the CD spectra of (R-MBA)Bi₄ film showed less than 20%

reduction of intensity (Figure S6b). These data indicate the good environmental stability of our chiral compounds, much better than the easily oxidized Ge²⁺-based NLO materials.⁴⁹ Moreover, Bi element can meet environmental protection requirements better than toxic Pb element.⁵⁰ On the other hand, the laser damage threshold of the (R-MBA)Bi₄ film (Figure S6c) was determined to be 0.17 J cm⁻² (170 W cm⁻²) at 1200 nm, which is better than that of the reported chiral hybrid lead halides (0.52 mJ cm⁻², 8.6 × 10⁴ W cm⁻² at 850 nm)¹⁴ but much less than that of standard inorganic NLO materials like LiNbO₃ (3 J cm⁻², 4.3 × 10⁸ W cm⁻² at 1064 nm).^{28,51} The relatively low optical damage threshold of our chiral films may be affected by their thermal stability, linear absorption of NLO signals, and grain boundary defects. The decompose temperature of (R-MBA)Bi₄ was about 489 K (Figure S6d), which is lower than the high melting point of LiNbO₃ (reach 1530 K).²⁸ Furthermore, due to the high absorption coefficient of (R-MBA)Bi₄ at 400 nm (1.8 × 10⁵ cm⁻¹), the absorption of the output THG signals might also contribute part of the optical damage energy. Hence, our chiral compounds show potential in ultrathin and low power NLO devices.

CONCLUSIONS

Our present work demonstrated the resonantly enhanced SHG and THG responses of chiral (R-MBA)Bi₄ films. Since broad STE exciton, strong FE, and discrete CB energy levels are often discovered in other low-dimensional chiral hybrid metal halides, our findings may trigger interest in the exploration of their SHG and THG resonance effect. The key points of the exploration are to select samples with suitable thickness and to perform systematic measurements in different excitation wavelength. Today, with the rapid development of optoelectronic technology, the functional demands for NLO materials are increasing. Solution-processed flexibility makes chiral hybrid metal halides suitable for versatile miniaturized and integrated optical design on arbitrary substrate.⁵² The development of chiral hybrid metal halides, a new type of NLO materials, promotes the evolution of nonlinear optoelectronic information technology and material science.

ASSOCIATED CONTENT

Supporting Information

The Supporting Information is available free of charge at <https://pubs.acs.org/doi/10.1021/jacs.1c06567>.

Experimental methods, crystal pictures, simulated powder XRD patterns, twisted R-MBA⁺ and S-MBA⁺ in crystal structures, schematic setup for wavelength-dependent NLO measurement, ambient stability of powder XRD and CD, laser damage threshold, TG/DSC, optical image and Raman spectrum of exfoliated monolayer WS₂, crystallographic data, selected bond distances and angles, and n and κ values of (R-MBA)Bi₄ film; notes on polarization-dependent SHG and THG, thickness-dependent SHG and THG in a lossy medium, and quantification of the SHG and THG susceptibilities (PDF)

Accession Codes

CCDC 2093394 and 2093395 contain the supplementary crystallographic data for this paper. These data can be obtained free of charge via www.ccdc.cam.ac.uk/data_request/cif, or by emailing data_request@ccdc.cam.ac.uk, or by contacting The

Cambridge Crystallographic Data Centre, 12 Union Road, Cambridge CB2 1EZ, UK; fax: +44 1223 336033.

AUTHOR INFORMATION

Corresponding Authors

Li Yao – Wuhan National Laboratory for Optoelectronics, Huazhong University of Science and Technology, Wuhan 430074, China; orcid.org/0000-0002-1923-1285; Email: yl4535467@gmail.com

Jian Wang – Wuhan National Laboratory for Optoelectronics, Huazhong University of Science and Technology, Wuhan 430074, China; orcid.org/0000-0002-0579-3041; Email: jwang@hust.edu.cn

Authors

Zhouxiaosong Zeng – Key Laboratory for Micro-Nano Physics and Technology of Hunan Province, School of Physics and Electronics, Hunan University, Changsha 410006, China

Chengkun Cai – Wuhan National Laboratory for Optoelectronics, Huazhong University of Science and Technology, Wuhan 430074, China

Peng Xu – Research Institute for Magnetolectronics & Weak Magnetic-field Detection, College of Science, China Three Gorges University, Yichang 443002, China; orcid.org/0000-0001-6023-136X

Honggang Gu – State Key Laboratory of Digital Manufacturing Equipment and Technology, Huazhong University of Science and Technology, Wuhan 430074, China; orcid.org/0000-0001-8812-1621

Liang Gao – Wuhan National Laboratory for Optoelectronics, Huazhong University of Science and Technology, Wuhan 430074, China

Junbo Han – Wuhan National High Magnetic Field Center, Huazhong University of Science and Technology, Wuhan 430074, China; orcid.org/0000-0002-5072-4897

Xiaowei Zhang – International Center for Quantum Materials, School of Physics, Peking University, Beijing 100871, China

Xi Wang – Wuhan National Laboratory for Optoelectronics, Huazhong University of Science and Technology, Wuhan 430074, China

Xiao Wang – Key Laboratory for Micro-Nano Physics and Technology of Hunan Province, School of Physics and Electronics, Hunan University, Changsha 410006, China; orcid.org/0000-0002-2973-8215

Anlian Pan – College of Materials Science and Engineering, Hunan University, Changsha 410006, China; orcid.org/0000-0003-3335-3067

Wenxi Liang – Wuhan National Laboratory for Optoelectronics, Huazhong University of Science and Technology, Wuhan 430074, China

Shiyuan Liu – Wuhan National Laboratory for Optoelectronics, State Key Laboratory of Digital Manufacturing Equipment and Technology, and Wuhan National High Magnetic Field Center, Huazhong University of Science and Technology, Wuhan 430074, China; orcid.org/0000-0002-0756-1439

Chao Chen – Wuhan National Laboratory for Optoelectronics and School of Optical and Electronic Information, Huazhong University of Science and Technology, Wuhan 430074, China

Jiang Tang – Wuhan National Laboratory for Optoelectronics and School of Optical and Electronic Information, Huazhong

University of Science and Technology, Wuhan 430074, China; orcid.org/0000-0003-2574-2943

Complete contact information is available at: <https://pubs.acs.org/10.1021/jacs.1c06567>

Notes

The authors declare no competing financial interest.

ACKNOWLEDGMENTS

This work was financially supported by the National Natural Science Foundation of China (61725401, 51761145048, 61904058, and 11774116), the Major State Basic Research Development Program of China (2016YFB0700702), and Fundamental Research Funds for the Central Universities (2021XXJS028, 2019kfyRCPY037). The authors are grateful to the Analytical and Testing Center of HUST and for facility support of the Center for Nanoscale Characterization and Devices, WNLO. We thank Y. J. Shi (HUST) for their help for NLO measurement. We thank Prof. W. W. Liu (HUST) for useful discussion about nonlinear harmonic generation.

ABBREVIATIONS

GS, ground state; FE, free exciton; STE, self-trapped exciton; NLO, nonlinear optical; CB, conduction band; VB, valence band; 0–3D, 0–3-dimensional; SHG, second harmonic generation; THG, third harmonic generation; Abs, absorption; PL, photoluminescence; CD, circular dichroism; XRD, X-ray diffraction

REFERENCES

- (1) Boyd, R. W. *Nonlinear Optics*; Academic Press: 2008.
- (2) Maiman, T. H. Stimulated Optical Radiation in Ruby. *Nature* **1960**, *187*, 493–494.
- (3) Franken, P. A.; Hill, A. E.; Peters, C. W.; Weinreich, G. Generation of Optical Harmonics. *Phys. Rev. Lett.* **1961**, *7*, 118–119.
- (4) Braune, M.; Maiwald, M.; Eppich, B.; Brox, O.; Ginolas, A.; Sumpf, B.; Tränkle, G. Design and Realization of a Miniaturized DFB Diode Laser-Based SHG Light Source With a 2-nm Tunable Emission at 488 nm. *IEEE Trans. Compon., Packag., Manuf. Technol.* **2017**, *7*, 720–725.
- (5) Li, G.; Chen, Y.; Jiang, H.; Chen, X. Broadband sum-frequency generation using d33 in periodically poled LiNbO₃ thin film in the telecommunications band. *Opt. Lett.* **2017**, *42*, 939–942.
- (6) Lv, T.; Huang, Z.-F.; Wang, H.-W.; Lin, J.-Q.; Chen, G.-N.; Chen, X.-W.; Chen, R.; Huang, Z.; Wang, X.-L. Evaluation of collagen alteration after topical photodynamic therapy (PDT) using second harmonic generation (SHG) microscopy – in vivo study in a mouse model. *Photodiagn. Photodyn. Ther.* **2012**, *9*, 164–169.
- (7) Hopkins, F. K. Military laser applications: providing focus to nonlinear optics R&D. *Opt. Photonics News* **1998**, *9*, 32.
- (8) Boyd, G. D.; Miller, R. C.; Nassau, K.; Bond, W. L.; Savage, A. LiNbO₃: an efficient phase matchable nonlinear optical material. *Appl. Phys. Lett.* **1964**, *5*, 234–236.
- (9) Eckardt, R. C.; Masuda, H.; Fan, Y. X.; Byer, R. L. Absolute and relative nonlinear optical coefficients of KDP, KD*P, BaB₂O₄, LiIO₃, MgO:LiNbO₃, and KTP measured by phase-matched second-harmonic generation. *IEEE J. Quantum Electron.* **1990**, *26*, 922–933.
- (10) Eaton, D. F. Nonlinear optical materials. *Science* **1991**, *253*, 281–7.
- (11) Lee, M. M.; Teuscher, J.; Miyasaka, T.; Murakami, T. N.; Snaith, H. J. Efficient hybrid solar cells based on meso-superstructured organometal halide perovskites. *Science* **2012**, *338*, 643–7.
- (12) Jeong, M.; Choi, I. W.; Go, E. M.; Cho, Y.; Kim, M.; Lee, B.; Jeong, S.; Jo, Y.; Choi, H. W.; Lee, J.; Bae, J. H.; Kwak, S. K.; Kim, D.

S.; Yang, C. Stable perovskite solar cells with efficiency exceeding 24.8% and 0.3-V voltage loss. *Science* **2020**, *369*, 1615–1620.

(13) Huang, J.; Yuan, Y.; Shao, Y.; Yan, Y. Understanding the physical properties of hybrid perovskites for photovoltaic applications. *Nat. Rev. Mater.* **2017**, *2*, 17042.

(14) Yuan, C.; Li, X.; Semin, S.; Feng, Y.; Rasing, T.; Xu, J. Chiral Lead Halide Perovskite Nanowires for Second-Order Nonlinear Optics. *Nano Lett.* **2018**, *18*, 5411–5417.

(15) Guo, Z.; Li, J.; Wang, C.; Liu, R.; Liang, J.; Gao, Y.; Cheng, J.; Zhang, W.; Zhu, X.; Pan, R.; He, T. Giant Optical Activity and Second Harmonic Generation in 2D Hybrid Copper Halides. *Angew. Chem., Int. Ed.* **2021**, *60*, 8441–8445.

(16) Moon, T. H.; Oh, S. J.; Ok, K. M. $[(R)\text{-C}_8\text{H}_{12}\text{N}_4][\text{Bi}_2\text{Br}_{10}]$ and $[(S)\text{-C}_8\text{H}_{12}\text{N}_4][\text{Bi}_2\text{Br}_{10}]$: Chiral Hybrid Bismuth Bromides Templated by Chiral Organic Cations. *ACS Omega* **2018**, *3*, 17895–17903.

(17) Dehnhardt, N.; Axt, M.; Zimmermann, J.; Yang, M.; Mette, G.; Heine, J. Band Gap-Tunable, Chiral Hybrid Metal Halides Displaying Second-Harmonic Generation. *Chem. Mater.* **2020**, *32*, 4801–4807.

(18) Baikie, T.; Fang, Y.; Kadro, J. M.; Schreyer, M.; Wei, F.; Mhaisalkar, S. G.; Graetzel, M.; White, T. J. Synthesis and crystal chemistry of the hybrid perovskite $(\text{CH}_3\text{NH}_3)\text{PbI}_3$ for solid-state sensitized solar cell applications. *J. Mater. Chem. A* **2013**, *1*, 5628.

(19) Frohna, K.; Deshpande, T.; Harter, J.; Peng, W.; Barker, B. A.; Neaton, J. B.; Louie, S. G.; Bakr, O. M.; Hsieh, D.; Bernardi, M. Inversion symmetry and bulk Rashba effect in methylammonium lead iodide perovskite single crystals. *Nat. Commun.* **2018**, *9*, 1829.

(20) Long, G.; Sabatini, R.; Saidaminov, M. I.; Lakhwani, G.; Rasmata, A.; Liu, X.; Sargent, E. H.; Gao, W. Chiral-perovskite optoelectronics. *Nat. Rev. Mater.* **2020**, *5*, 423–439.

(21) Akkerman, Q. A.; Manna, L. What Defines a Halide Perovskite? *ACS Energy Lett.* **2020**, *5*, 604–610.

(22) Mercier, N. Hybrid Halide Perovskites: Discussions on Terminology and Materials. *Angew. Chem., Int. Ed.* **2019**, *58*, 17912–17917.

(23) Ma, J.; Fang, C.; Chen, C.; Jin, L.; Wang, J.; Wang, S.; Tang, J.; Li, D. Chiral 2D Perovskites with a High Degree of Circularly Polarized Photoluminescence. *ACS Nano* **2019**, *13*, 3659–3665.

(24) Li, L. S.; Tan, Y. H.; Wei, W. J.; Gao, H. Q.; Tang, Y. Z.; Han, X. B. Chiral Switchable Low-Dimensional Perovskite Ferroelectrics. *ACS Appl. Mater. Interfaces* **2021**, *13*, 2044–2051.

(25) Ishii, A.; Miyasaka, T. Direct detection of circular polarized light in helical 1D perovskite-based photodiode. *Sci. Adv.* **2020**, *6*, eabd3274.

(26) Chen, C.; Gao, L.; Gao, W.; Ge, C.; Du, X.; Li, Z.; Yang, Y.; Niu, G.; Tang, J. Circularly polarized light detection using chiral hybrid perovskite. *Nat. Commun.* **2019**, *10*, 1927.

(27) Long, G.; Jiang, C.; Sabatini, R.; Yang, Z.; Wei, M.; Quan, L. N.; Liang, Q.; Rasmata, A.; Askerka, M.; Walters, G.; Gong, X.; Xing, J.; Wen, X.; Quintero-Bermudez, R.; Yuan, H.; Xing, G.; Wang, X. R.; Song, D.; Voznyy, O.; Zhang, M.; Hoogland, S.; Gao, W.; Xiong, Q.; Sargent, E. H. Spin control in reduced-dimensional chiral perovskites. *Nat. Photonics* **2018**, *12*, 528–533.

(28) Nikogosyan, D. N. *Nonlinear Optical Crystals: A Complete Survey*; Springer: 2005.

(29) Wang, G.; Marie, X.; Gerber, I.; Amand, T.; Lagarde, D.; Bouet, L.; Vidal, M.; Balocchi, A.; Urbaszek, B. Giant enhancement of the optical second-harmonic emission of WSe_2 monolayers by laser excitation at exciton resonances. *Phys. Rev. Lett.* **2015**, *114*, 097403.

(30) Xiao, Z.; Song, Z.; Yan, Y. From Lead Halide Perovskites to Lead-Free Metal Halide Perovskites and Perovskite Derivatives. *Adv. Mater.* **2019**, *31*, 1803792.

(31) Abdelwahab, I.; Grinblat, G.; Leng, K.; Li, Y.; Chi, X.; Rusydi, A.; Maier, S. A.; Loh, K. P. Highly Enhanced Third-Harmonic Generation in 2D Perovskites at Excitonic Resonances. *ACS Nano* **2018**, *12*, 644–650.

(32) Saouma, F. O.; Stoumpos, C. C.; Wong, J.; Kanatzidis, M. G.; Jang, J. I. Selective enhancement of optical nonlinearity in two-

dimensional organic-inorganic lead iodide perovskites. *Nat. Commun.* **2017**, *8*, 742.

(33) Sun, B.; Liu, X.-F.; Li, X.-Y.; Zhang, Y.; Shao, X.; Yang, D.; Zhang, H.-L. Two-Dimensional Perovskite Chiral Ferromagnets. *Chem. Mater.* **2020**, *32*, 8914–8920.

(34) Perdew, J. P.; Burke, K.; Ernzerhof, M. Generalized Gradient Approximation Made Simple. *Phys. Rev. Lett.* **1996**, *77*, 3865–3868.

(35) Mitzi, D. B.; Brock, P. Structure and optical properties of several organic-inorganic hybrids containing corner-sharing chains of bismuth iodide octahedra. *Inorg. Chem.* **2001**, *40*, 2096–104.

(36) Ahn, J.; Lee, E.; Tan, J.; Yang, W.; Kim, B.; Moon, J. A new class of chiral semiconductors: chiral-organic-molecule-incorporating organic-inorganic hybrid perovskites. *Mater. Horiz.* **2017**, *4*, 851–856.

(37) Ben-Moshe, A.; Teitelboim, A.; Oron, D.; Markovich, G. Probing the Interaction of Quantum Dots with Chiral Capping Molecules Using Circular Dichroism Spectroscopy. *Nano Lett.* **2016**, *16*, 7467–7473.

(38) Purdie, N.; Brittain, H. G. *Analytical Applications of Circular Dichroism*; Elsevier: 1994.

(39) Kentsch, R.; Morgenroth, M.; Scholz, M.; Xu, K.; Schmedt Auf der Gunne, J.; Lenzer, T.; Oum, K. Direct Observation of the Exciton Self-Trapping Process in CsCu_2I_3 Thin Films. *J. Phys. Chem. Lett.* **2020**, *11*, 4286–4291.

(40) McCall, K. M.; Stoumpos, C. C.; Kostina, S. S.; Kanatzidis, M. G.; Wessels, B. W. Strong Electron-Phonon Coupling and Self-Trapped Excitons in the Defect Halide Perovskites $\text{A}_3\text{M}_2\text{I}_9$ (A = Cs, Rb; M = Bi, Sb). *Chem. Mater.* **2017**, *29*, 4129–4145.

(41) Li, T.; Chen, X.; Wang, X.; Lu, H.; Yan, Y.; Beard, M. C.; Mitzi, D. B. Origin of Broad-Band Emission and Impact of Structural Dimensionality in Tin-Alloyed Ruddlesden-Popper Hybrid Lead Iodide Perovskites. *ACS Energy Lett.* **2020**, *5*, 347–352.

(42) Luo, J.; Wang, X.; Li, S.; Liu, J.; Guo, Y.; Niu, G.; Yao, L.; Fu, Y.; Gao, L.; Dong, Q.; Zhao, C.; Leng, M.; Ma, F.; Liang, W.; Wang, L.; Jin, S.; Han, J.; Zhang, L.; Etheridge, J.; Wang, J.; Yan, Y.; Sargent, E. H.; Tang, J. Efficient and stable emission of warm-white light from lead-free halide double perovskites. *Nature* **2018**, *563*, 541–545.

(43) Yin, X.; Ye, Z.; Chenet, D. A.; Ye, Y.; O'Brien, K.; Hone, J. C.; Zhang, X. Edge nonlinear optics on a MoS_2 atomic monolayer. *Science* **2014**, *344*, 488–90.

(44) Huang, C.; Gao, Y.; Wang, S.; Zhang, C.; Yi, N.; Xiao, S.; Song, Q. Giant blueshifts of excitonic resonances in two-dimensional lead halide perovskite. *Nano Energy* **2017**, *41*, 320–326.

(45) Saynatjoki, A.; Karvonen, L.; Rostami, H.; Autere, A.; Mehrahar, S.; Lombardo, A.; Norwood, R. A.; Hasan, T.; Peyghambarian, N.; Lipsanen, H.; et al. Ultra-strong nonlinear optical processes and trigonal warping in MoS_2 layers. *Nat. Commun.* **2017**, *8*, 893.

(46) Youngblood, N.; Peng, R.; Nemilentsau, A.; Low, T.; Li, M. Layer-Tunable Third-Harmonic Generation in Multilayer Black Phosphorus. *ACS Photonics* **2017**, *4*, 8–14.

(47) Autere, A.; Jussila, H.; Marini, A.; Saavedra, J. R. M.; Dai, Y.; Säynätjoki, A.; Karvonen, L.; Yang, H.; Amirsolaimani, B.; Norwood, R. A.; Peyghambarian, N.; Lipsanen, H.; Kieu, K.; de Abajo, F. J. G.; Sun, Z. Optical harmonic generation in monolayer group-VI transition metal dichalcogenides. *Phys. Rev. B: Condens. Matter Mater. Phys.* **2018**, *98*, 115426.

(48) Janisch, C.; Wang, Y.; Ma, D.; Mehta, N.; Elias, A. L.; Perea-Lopez, N.; Terrones, M.; Crespi, V.; Liu, Z. Extraordinary Second Harmonic Generation in tungsten disulfide monolayers. *Sci. Rep.* **2015**, *4*, 5530.

(49) Stoumpos, C. C.; Frazer, L.; Clark, D. J.; Kim, Y. S.; Rhim, S. H.; Freeman, A. J.; Ketterson, J. B.; Jang, J. I.; Kanatzidis, M. G. Hybrid germanium iodide perovskite semiconductors: active lone pairs, structural distortions, direct and indirect energy gaps, and strong nonlinear optical properties. *J. Am. Chem. Soc.* **2015**, *137*, 6804–19.

(50) Wani, A. L.; Ara, A.; Usmani, J. A. Lead toxicity: a review. *Interdiscip. Toxicol.* **2015**, *8*, 55–64.

(51) Myers, L. E.; Miller, G. D.; Eckardt, R. C.; Fejer, M. M.; Byer, R. L.; Bosenberg, W. R. Quasi-phase-matched 1.064-microm-pumped optical parametric oscillator in bulk periodically poled LiNbO₃. *Opt. Lett.* **1995**, *20*, 52–4.

(52) Tumuluri, A.; Bharati, M.S.S.; Rao, S. V.; James Raju, K.C. Structural, optical and femtosecond third-order nonlinear optical properties of LiNbO₃ thin films. *Mater. Res. Bull.* **2017**, *94*, 342–351.

Supplementary Information

Strong Second- and Third-Harmonic Generation in 1D Chiral Hybrid

Bismuth Halides

Li Yao^{1*}, Zhouxiaosong Zeng², Chengkun Cai¹, Peng Xu³, Honggang Gu⁴, Liang Gao¹, Junbo Han⁵, Xiaowei Zhang⁶, Xi Wang¹, Xiao Wang², Anlian Pan⁷, Jian Wang^{1*}, Wenxi Liang¹, Shiyuan Liu^{1,4,5}, Chao Chen^{1,8}, Jiang Tang^{1,8}

¹Wuhan National Laboratory for Optoelectronics, Huazhong University of Science and Technology, Wuhan 430074, China

²Key Laboratory for Micro-Nano Physics and Technology of Hunan Province, School of Physics and Electronics, Hunan University, Changsha 410006, China

³Research Institute for Magnetolectronics & Weak Magnetic-field Detection, College of Science, China Three Gorges University, Yichang 443002, China

⁴State Key Laboratory of Digital Manufacturing Equipment and Technology, Huazhong University of Science and Technology, Wuhan 430074, China

⁵Wuhan National High Magnetic Field Center, Huazhong University of Science and Technology, Wuhan 430074, China

⁶International Center for Quantum Materials, School of Physics, Peking University, Beijing 100871, China

⁷College of Materials Science and Engineering, Hunan University, Changsha 410006, China

⁸School of Optical and Electronic Information, Huazhong University of Science and Technology, Wuhan 430074, China

*Corresponding authors: yl4535467@gmail.com; jwang@hust.edu.cn

Experimental methods

Synthesis. R-(+)- α -Methylbenzylamine (R-MBA, 99% gas chromatography purity, 98% enantiomeric excess), S-(-)- α -Methylbenzylamine (S-MBA, >99% gas chromatography purity), N,N-anhydrous dimethylformamide (DMF, 99.8%), bismuth trioxide (Bi_2O_3 , 99.99%) were purchased from Aladdin (Shanghai, China). Aqueous hydriodic acid 45% was purchased from Sinopharm Chemical Reagent Company, Ltd. All materials and reagents were used as received. In a 50 mL glass bottle, Bi_2O_3 (2.796 g, 6 mmol) and R- or S-MBA (1.527 mL, 12 mmol) were dissolved in 20 mL aqueous HI solution (without hypophosphorous acid). After a tight seal, the bottle was placed in an oven (Mettler, atmoCONTROL). First, the oven was kept at 120 °C for 6 h for Bi_2O_3 to fully dissolved and then was slowly cooled to room temperature with a falling rate of about 3 °C per hour. After these procedures, the red (R-MBA) BiI_4 crystals were formed. The crystals should be immediately filtered and washed with hexane, and thoroughly dried on a hotplate at 90 °C for 30 mins. Yield 6 g (60% based on total Bi content).

Perovskite film preparation. The chiral perovskite films were fabricated by a one-step spin coating method. (R- or S-MBA) BiI_4 single crystals were dissolved in DMF with desired concentrations (depending on the desired film thicknesses, for example, 0.1 mM for ~ 55 nm, 0.2 mM for ~90 nm, and 0.3 mM for ~145 nm, etc.) as precursor solutions. The substrates (quartz for absorption and CD measurements, and glasses for SHG and THG measurements) were cleaned by sonication in acetone, ethanol, and deionized water sequentially. Before the spin-coating process, the substrates were treated by O_2 plasma for 5 min. Then the (R- or S-MBA) BiI_4 precursor solutions were spin-coated onto the substrates at 2000 rpm for 40 s. Finally, the (R- or S-MBA) BiI_4 films were annealed at 90 °C for 20 min to crystallize.

Characterization. Single crystal X-ray diffraction (XRD) patterns were collected using an XtaLAB PRO MM007HF diffractometer at room temperature with Cu K α radiation ($\lambda=1.54184 \text{ \AA}$). The crystal data were collected by CrysAlisPro 1.171.39.28b program (Rigaku Oxford Diffraction, 2015). Empirical absorption corrections were performed using spherical harmonics, implemented in SCALE3 ABSPACK scaling algorithm. The structures were solved using intrinsic phasing method and refined by full-matrix least-squares techniques using the SHELX software

package¹⁻³ within the OLEX2 suite⁴. Pictures of the crystal structures were created using VESTA software⁵. Powder and film XRD patterns were obtained by Philips X'pert pro MRD diffractometer using Cu K α radiation. Thermogravimetric analysis (TG) and differential scanning calorimetry (DSC) analyses were performed on a PerkinElmer Diamond TG/DTA6300 system from room temperature to 600 °C with a heating rate of 10 °C per min in N₂ flow. Transmission CD spectra were collected using a CD spectrometer (J810, JASCO). Absorption spectra were measured on a UV-vis spectrophotometer (PerkinElmer Instruments, Lambda 950) using an integrating sphere. The refractive index and extinction coefficient were determined by a spectroscopic ellipsometer⁶ (ME-L, Wuhan Eoptics Technology Co., Ltd) at reflection measurement mode with an incident angle set at 65°. Photoluminescence spectra were measured by a self-built light path equipped with a 365 nm laser source and liquid helium temperature control system. The atomic force microscope (AFM) images were collected by a SPM-9700 AFM (Shimadzu Co., Japan).

Nonlinear optical measurement. For wavelength-dependent measurement, a home-built light path was utilized. The details on how the NLO Intensity was measured were provided in Figure S3.

For mapping and film thickness-dependent nonlinear measurement, a microscopic optical system was utilized. The pump laser was generated by a mode-locked Ti: sapphire laser (Tsunami) at 800 nm (pulse width of 80 fs, repetition frequency of 80 MHz), which was amplified by a regenerative amplifier laser (Spitfire Ace 100, 1 kHz) and then introduced into an optical parameter amplifier (OPA, TOPAS Prime). The mean power was about 10 μ W. The output laser from the OPA was fixed at 1200 nm used for nonlinear optical measurements. SHG and THG signals were collected in transmission geometry. The numerical aperture of the 20 \times objective was 0.55. The corresponding spot size was \sim 3 μ m in diameter. For the SHG and THG mapping, the image was smooth scanned, and the integration time of each point is 0.13 s. For the calibration of nonlinear susceptibility, X-cut lithium niobate single crystal film (600 nm LiNbO₃ on 2.006 μ m SiO₂s/500 μ m quartz substrate) was purchased from Jinan Jingzheng Electronics Co.; the single-layer WS₂ were mechanically exfoliated from single-crystal WS₂ onto glass slides.

Computational methods. The first-principles calculations were performed within the

framework of the density functional theory (DFT) using the VASP code⁷⁻⁸. The projector augmented-wave (PAW)⁹⁻¹⁰ method was employed with an energy cutoff of 400 eV for the plane-wave basis set. For the exchange-correlation potential, we used the Perdew Burke Ernzerhof (PBE)¹¹ form of the generalized gradient approximation. All the lattice parameters and atomic coordinates were fully relaxed until the forces on atoms were below 0.01 eV/Å. A 5×3×1 k-mesh in the Brillouin zone has been used for integration. Due to the heavy Bi element, the effect of spin-orbital coupling (SOC) was included.

Supplementary Figures

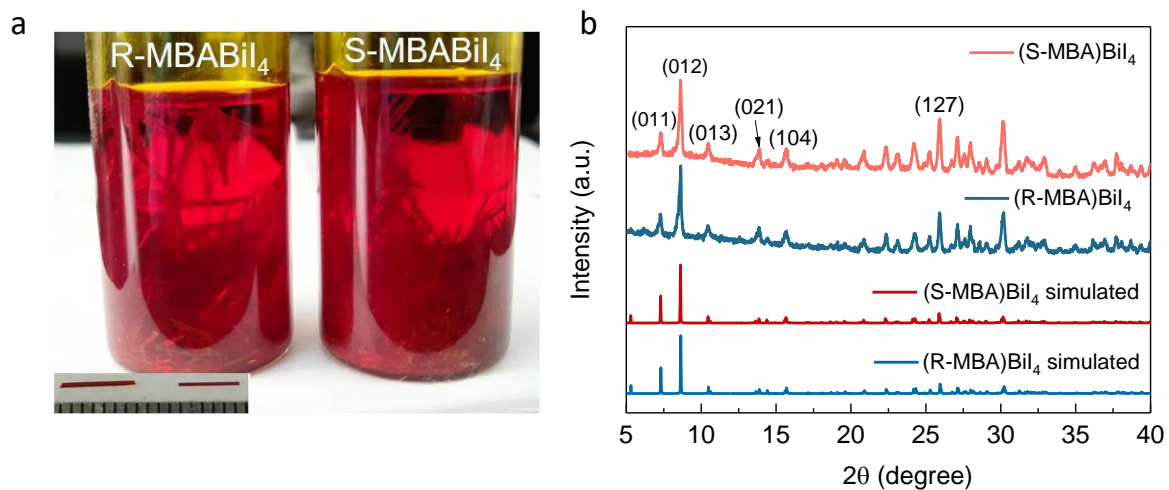


Figure S1. (a) (R-MBA)BiI₄ and (S-MBA)BiI₄ single crystals grown in HI acid. The inset shows the grown red single crystals (about 5 mm long). (b). Powder XRD patterns of (R-MBA)BiI₄ and (S-MBA)BiI₄ powder. The simulated powder XRD patterns are shown for reference. Miller indices are labeled to indicate the strongly preferred orientations.

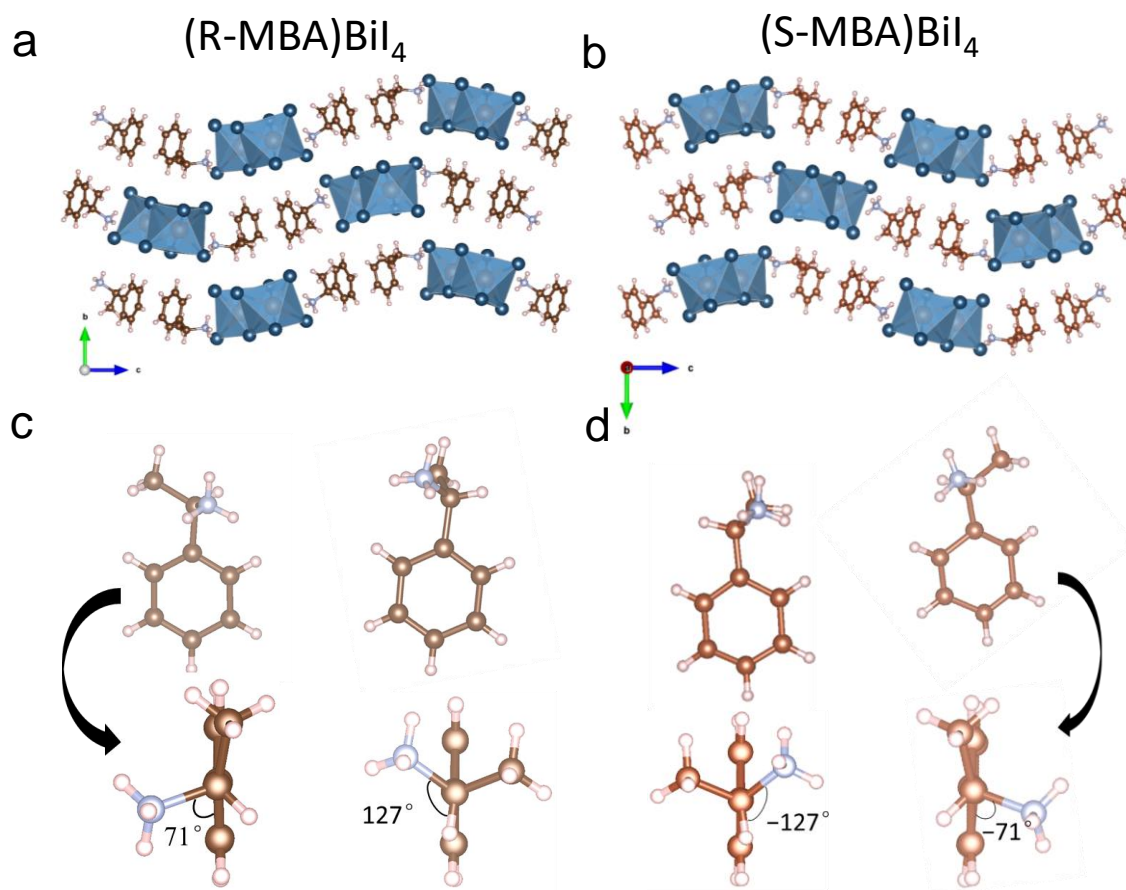


Figure S2. Crystal structures of (a) (R-MBA)BiI₄ and (b) (S-MBA)BiI₄ projected along a-axis. (c) Twisted R-MBA⁺ in (R-MBA)BiI₄ and (d) twisted S-MBA⁺ in (S-MBA)BiI₄ are presented to visualize their distortion.

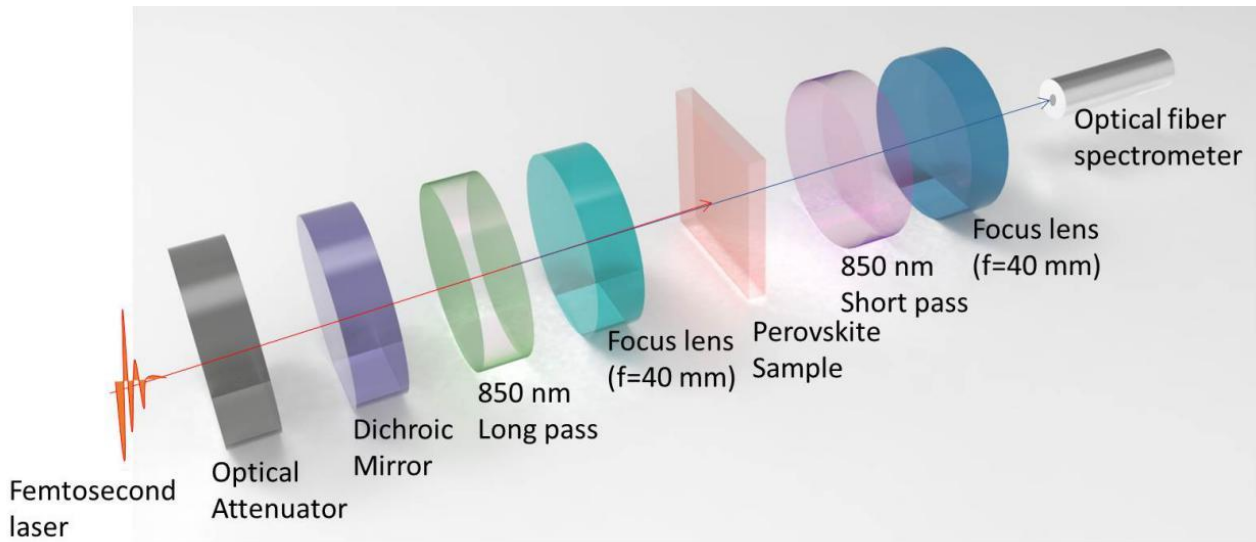


Figure S3. Schematic setup for the wavelength-dependence nonlinear optical measurements. The pump laser was generated by a diode pumped solid state femtosecond laser (COHERENT) at 804 nm (pulse width of 34.56 fs, a bandwidth of 31.44 nm, repetition frequency of 5 kHz). An optical parameter amplifier (OPA, ORPHEUS+Lyra SH/DFP) was utilized to obtain a variety of coherent pump wavelengths spanning from 1200 nm to 1650 nm at increments of 25 nm. The long pass dichroic mirror (Thorlabs DMLP1150B) and an 850 nm long-pass filter (FEL0850) were used to filter out visible light produced by OPA. The incident laser energy was tuned by optical attenuator and was measured by a germanium photodetector (Thorlabs). Then the incident laser was focused onto the film samples by a near-IR focus lens ($f=40$ mm). The nonlinear emission was collected in transmitted configuration. The 850 nm short-pass filter (FES0850) was used to filter out the IR laser. The SHG and THG signal passed through a visible focus lens ($f=40$ mm) and then detected by an optical fiber spectrometer (Ocean Optics). During the wavelength-dependence SHG and THG measurement, the pump power was fixed at 100 mW; the light path and sample position remained unchanged.

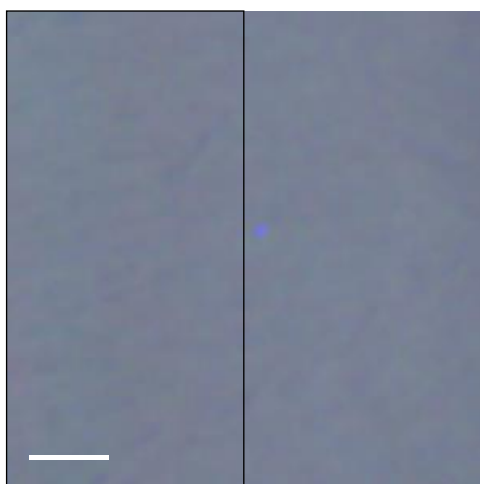


Figure S4. The optical image of the same region for SHG and THG mapping of (R-MBA)BiI₄ film in Figure 4d. The corresponding area is marked out by a black frame. Scale bar: 5 μm.

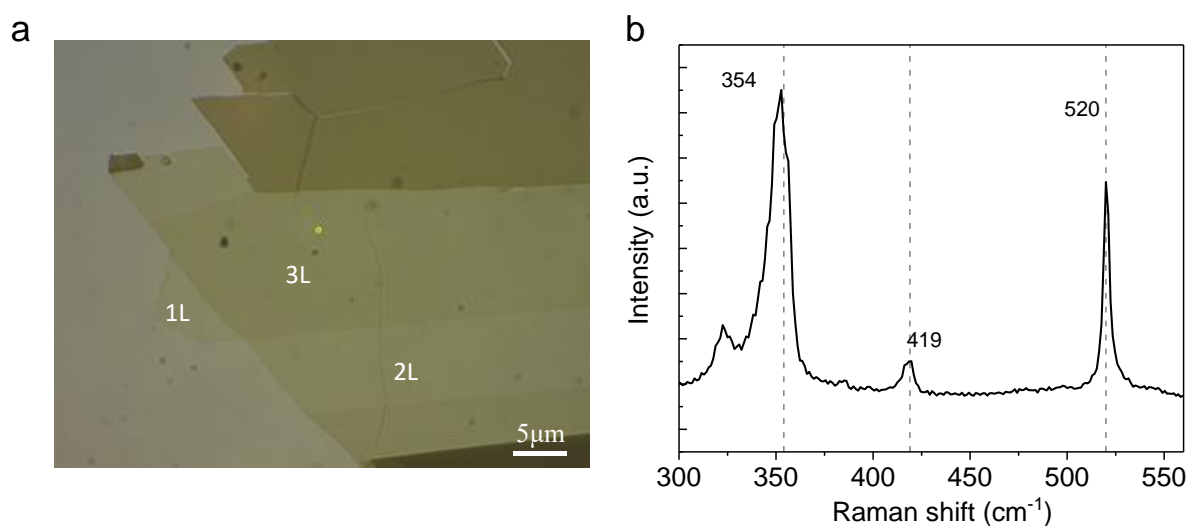


Figure S5. (a) The optical image of mechanical exfoliated WS₂ film on a glass substrate. Here, 1L, 2L, and 3L denote single layer, double layer, and three-layer. (b) Raman spectrum (with 514 nm laser excitation) of the 1L WS₂ film verifies its single-layer structure.¹²

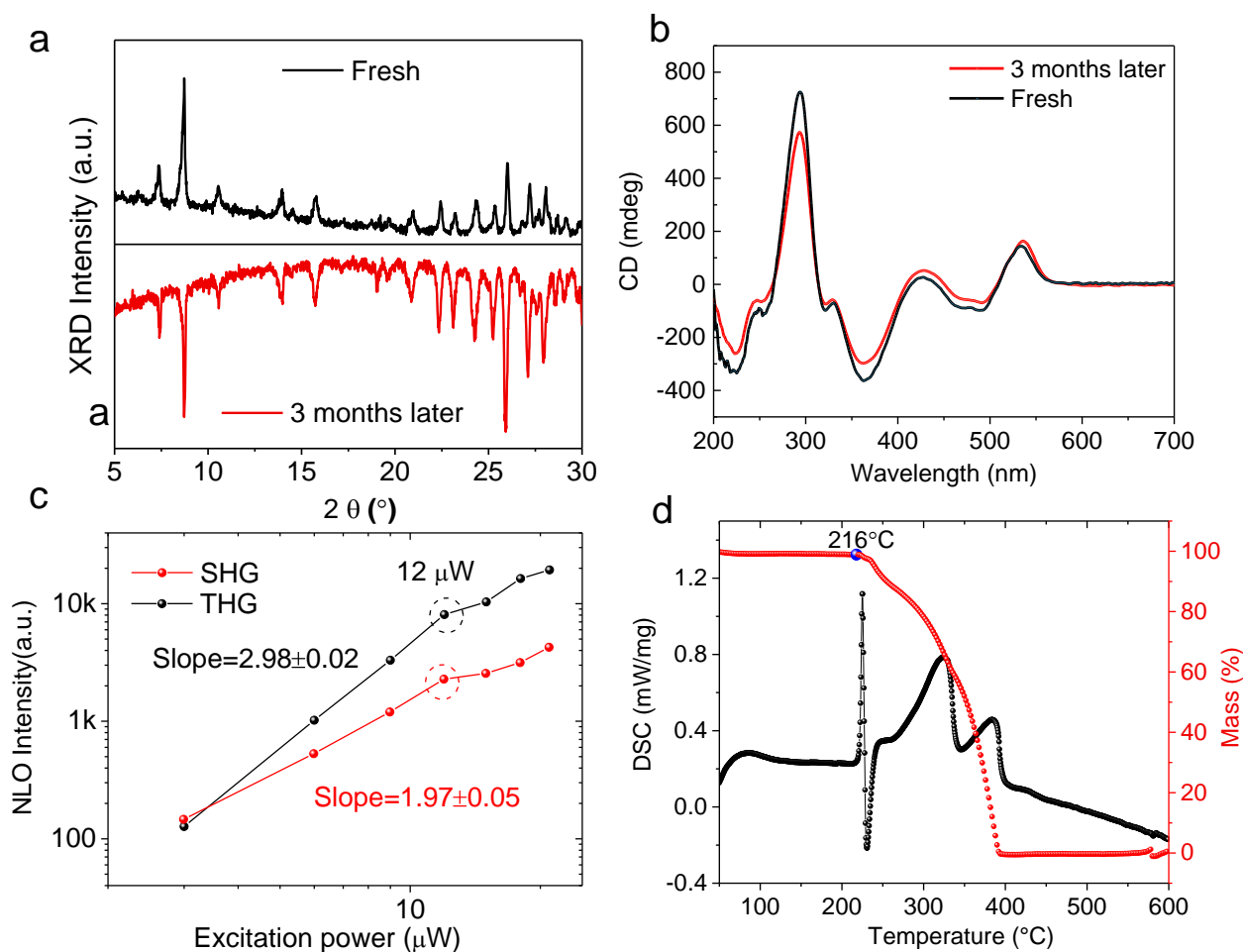


Figure S6. (a) Powder XRD patterns of (R-MBA)Bi₄ powder and (b) CD patterns of (R-MBA)Bi₄ film freshly prepared and exposed to ambient condition for 3 months, respectively. (c) Power dependence of SHG and THG intensities detected from (R-MBA)Bi₄ film using the microscopic NLO test system. The excitation laser is 1200 nm (80 fs, 1k Hz). The data are plotted on a log-log scale. When the pump power is lower than 12 μW , the SHG and THG dependences on the pump power follow quadratic and cubic trends, respectively. The laser damage threshold was determined to be 170 mJ cm⁻² for a pulse power, corresponding to mean power of around 170 W cm⁻². The laser spot diameter of ~ 3 μm . (d) TG and DSC spectra of (R-MBA)Bi₄ grounded powder. The results show no weight loss and no phase transition up to 216°C in (R-MBA)Bi₄, indicating its good thermal tolerance under common device operation.

Supplementary Tables

Table S1. Crystallographic data and structure refinement details for (R-MBA)BiI₄ and (S-MBA)BiI₄.

Compound	(S-MBA)BiI ₄	(R-MBA)BiI ₄
Empirical formula	C ₈ H ₁₂ BiI ₄ N	C ₈ H ₁₂ BiI ₄ N
Formula weight	838.77	838.77
Temperature/K	297.63(19)	294.9(3)
Crystal system	orthorhombic	orthorhombic
Space group	P2 ₁ 2 ₁ 2 ₁	P2 ₁ 2 ₁ 2 ₁
<i>a</i> /Å	7.69010(10)	7.68920(5)
<i>b</i> /Å	13.01490(10)	13.01898(6)
<i>c</i> /Å	33.3761(3)	33.37932(15)
α /°	90	90
β /°	90	90
γ /°	90	90
Volume/Å ³	3340.48(6)	3341.45(3)
<i>Z</i>	8	8
ρ_{calc} /cm ³	3.336	3.335
μ /mm ⁻¹	78.552	78.529
F(000)	2896.0	2896.0
Crystal size/mm ³	0.241 × 0.037 × 0.023	0.322 × 0.031 × 0.025
Radiation	CuK α (λ = 1.54184)	CuK α (λ = 1.54184)
2 θ range /°	7.29 to 114.992	5.296 to 148.002
Index ranges	-8 ≤ <i>h</i> ≤ 7 -14 ≤ <i>k</i> ≤ 14 -36 ≤ <i>l</i> ≤ 36	-8 ≤ <i>h</i> ≤ 9 -16 ≤ <i>k</i> ≤ 16 -41 ≤ <i>l</i> ≤ 41
Reflections collected	12466	82297
Independent reflections	4546 [<i>R</i> _{int} = 0.0713, <i>R</i> _{sigma} = 0.0581]	6721 [<i>R</i> _{int} = 0.0685, <i>R</i> _{sigma} = 0.0228]
Data/restraints/parameters	4546/0/257	6721/0/257
Goodness-of-fit on F ²	1.088	1.062
Final R indexes [<i>I</i> ≥ 2 σ (<i>I</i>)]	<i>R</i> ₁ = 0.0507, <i>wR</i> ₂ = 0.1334	<i>R</i> ₁ = 0.0235, <i>wR</i> ₂ = 0.0573
Final R indexes [all data]	<i>R</i> ₁ = 0.0521, <i>wR</i> ₂ = 0.1349	<i>R</i> ₁ = 0.0244, <i>wR</i> ₂ = 0.0576
Largest diff. peak/hole / (e Å ⁻³)	2.11/-1.90	1.16/-1.24
Flack parameter	0.04(3)	0.036(5)

Table S2. Selected bond lengths (Å) for (R-MBA)BiI₄ and (S-MBA)BiI₄.

(R-MBA)BiI ₄			(S-MBA)BiI ₄		
Atom	Atom	Length/Å	Atom	Atom	Length/ Å
Bi2	I2	3.0600(7)	Bi2	I2	3.0591(18)
Bi2	I3	3.1244(7)	Bi2	I3	3.1243(19)
Bi2	I4	3.2997(7)	Bi2	I4	3.2984(18)
Bi2	I5	3.2799(7)	Bi2	I5	3.2807(19)
Bi2	I7	2.9525(7)	Bi2	I7	2.9524(18)
Bi2	I8	2.9113(7)	Bi2	I8	2.9116(18)
Bi1	I2	3.2456(7)	Bi1	I2	3.2445(18)
Bi1	I3	3.2580(7)	Bi1	I3	3.2590(18)
Bi1	I4	3.0722(8)	Bi1	I4	3.0711(19)
Bi1	I5	3.0858(8)	Bi1	I5	3.0851(19)
Bi1	I6	2.9390(8)	Bi1	I6	2.9383(19)
Bi1	I1	2.9788(7)	Bi1	I1	2.9762(19)

Table S3. Selected bond angles (°) for (R-MBA)BiI₄ and (S-MBA)BiI₄.

(R-MBA)BiI ₄				(S-MBA)BiI ₄			
Atom	Atom	Atom	Angle/°	Atom	Atom	Atom	Angle/°
I2	Bi2	I3	172.09(2)	I2	Bi2	I3	172.03(5)
I2	Bi2	I4	94.633(19)	I2	Bi2	I4	94.72(5)
I2	Bi2	I5	86.326(18)	I2	Bi2	I5	86.30(5)
I3	Bi2	I4	85.722(18)	I3	Bi2	I4	85.70(5)
I3	Bi2	I5	85.896(19)	I3	Bi2	I5	85.87(5)
I5	Bi2	I4	82.241(19)	I5	Bi2	I4	82.25(5)
I7	Bi2	I2	89.74(2)	I7	Bi2	I2	89.82(5)
I7	Bi2	I3	98.17(2)	I7	Bi2	I3	98.15(5)
I7	Bi2	I4	87.29(2)	I7	Bi2	I4	87.30(5)
I7	Bi2	I5	168.47(2)	I7	Bi2	I5	168.51(6)
I8	Bi2	I2	93.28(2)	I8	Bi2	I2	93.30(6)
I8	Bi2	I3	86.48(2)	I8	Bi2	I3	86.40(5)
I8	Bi2	I4	172.08(2)	I8	Bi2	I4	171.98(6)
I8	Bi2	I5	98.55(2)	I8	Bi2	I5	98.55(5)
I8	Bi2	I7	92.48(2)	I8	Bi2	I7	92.47(6)
I2	Bi1	I3	83.103(18)	I2	Bi1	I3	83.09(5)
I4	Bi1	I2	94.240(19)	I4	Bi1	I2	94.23(5)
I4	Bi1	I3	87.304(19)	I4	Bi1	I3	87.26(5)
I4	Bi1	I5	174.27(2)	I4	Bi1	I5	174.26(6)
I5	Bi1	I2	86.506(18)	I5	Bi1	I2	86.51(5)
I5	Bi1	I3	87.15(2)	I5	Bi1	I3	87.18(5)
I6	Bi1	I2	89.91(2)	I6	Bi1	I2	89.99(5)
I6	Bi1	I3	171.29(2)	I6	Bi1	I3	171.30(6)
I6	Bi1	I4	88.04(2)	I6	Bi1	I4	88.00(5)
I6	Bi1	I5	97.65(2)	I6	Bi1	I5	97.70(6)
I6	Bi1	I1	91.74(2)	I6	Bi1	I1	91.69(6)
I1	Bi1	I2	172.46(2)	I1	Bi1	I2	172.45(6)
I1	Bi1	I3	95.86(2)	I1	Bi1	I3 ²	95.85(6)
I1	Bi1	I4	93.17(2)	I1	Bi1	I4	93.18(6)
I1	Bi1	I5	85.98(2)	I1	Bi1	I5	85.97(5)
Bi2	I2	Bi1	93.739(17)	Bi2	I2	Bi1	93.76(5)
Bi2	I3	Bi1	92.873(18)	Bi2	I3	Bi1	92.88(5)
Bi1	I4	Bi2	93.027(18)	Bi1	I4	Bi2	93.09(5)
Bi1	I5	Bi2 ²	92.582(18)	Bi1	I5	Bi2	92.57(5)

Table S4. The detailed n and κ values of (R-MBA)BiI₄ film at different wavelength λ (nm).

λ	n	κ	λ	n	κ	λ	n	κ
200	1.56877	0.65231	700	1.93254	0.000123	1200	1.79632	0.000007
225	1.55614	0.53613	725	1.91661	0.000098	1225	1.79283	0.000007
250	1.52615	0.64203	750	1.90318	0.000079	1250	1.78942	0.000006
275	1.69575	0.76639	775	1.89164	0.000065	1275	1.78607	0.000006
300	1.91287	0.61901	800	1.88155	0.000054	1300	1.78277	0.000005
325	1.87964	0.49566	825	1.87261	0.000046	1325	1.77952	0.000005
350	1.75434	0.44339	850	1.86459	0.000039	1350	1.77631	0.000005
375	1.82052	0.62135	875	1.85734	0.000033	1375	1.77313	0.000004
400	2.00984	0.58348	900	1.85072	0.000029	1400	1.76998	0.000004
425	2.05599	0.47431	925	1.84462	0.000025	1425	1.76685	0.000004
450	2.13506	0.40577	950	1.83896	0.000022	1450	1.76373	0.000004
475	2.08316	0.25297	975	1.83368	0.000019	1475	1.76062	0.000003
500	1.9716	0.30055	1000	1.82872	0.000017	1500	1.75752	0.000003
525	2.1401	0.46134	1025	1.82403	0.000015	1525	1.75443	0.000003
550	2.30315	0.14305	1050	1.81958	0.000013	1550	1.75134	0.000003
575	2.14895	0.01542	1075	1.81534	0.000012	1575	1.74824	0.000003
600	2.0582	0.000643	1100	1.81127	0.000011	1600	1.74514	0.000003
625	2.00925	0.00035	1125	1.80735	0.00001	1625	1.74203	0.000002
650	1.97646	0.000225	1150	1.80356	0.000009	1650	1.7389	0.000002
675	1.95194	0.000161	1175	1.79989	0.000008	1675	1.73577	0.000002

Supplementary Notes

Supplementary Note 1: polarization-dependent SHG and THG.

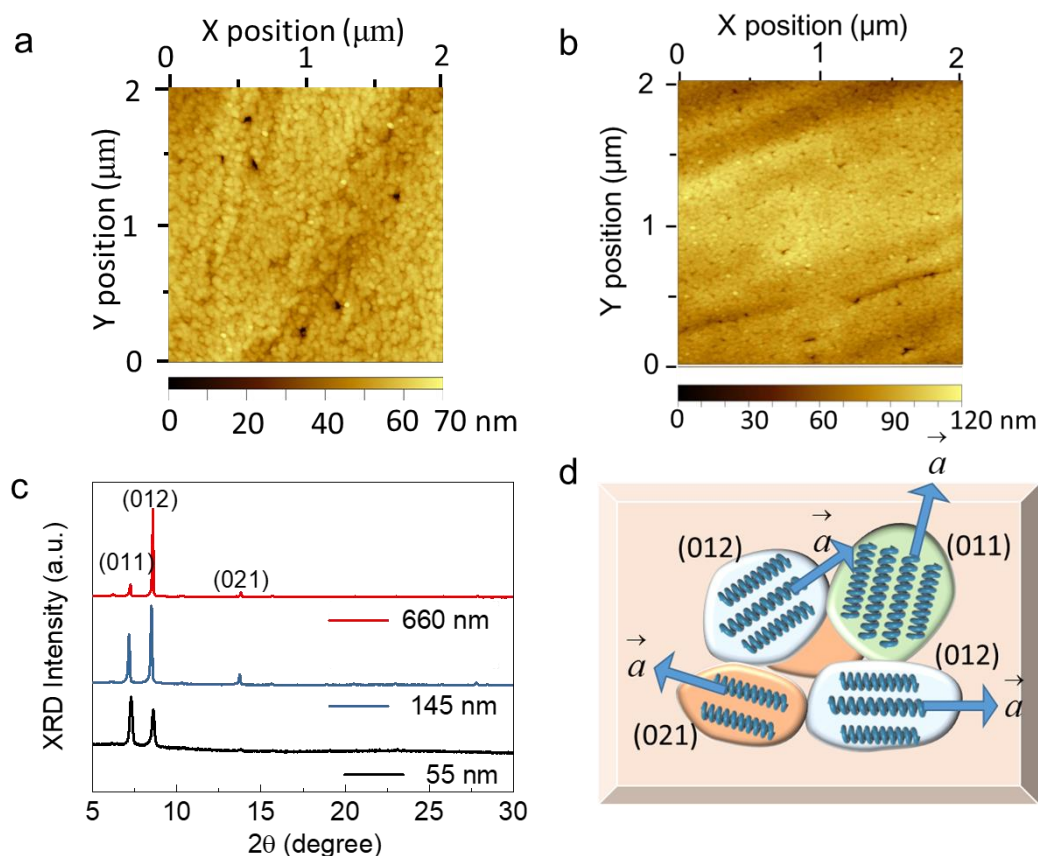


Figure S7. (a), AFM image of (R-MBA)Bi₄ film (~65 nm). (b), AFM image of (R-MBA)Bi₄ film (~145 nm). (c), XRD patterns of different thick (R-MBA)Bi₄ film. (d), A schematic represents selected grains in the polycrystalline film. Every grain could be a single crystal with a specific a-axis direction (denoted as an arrow) and crystal face (denoted as different crystal color).

The chiral (R-MBA)Bi₄ film is composed of a large number of single-crystal grains. As shown in the AFM images (**Figure S7a, b**), different thick films have similar grain size (spanning from 30 to 50 nm in diameter) and thickness fluctuations (average surface roughness Ra 4–4.85 nm). On the other hand, as shown in the XRD spectra (**Figure S7c**), different thick films all have three remained reflections ((011), (012), and (021)), which indicate that the grown films are mainly composed of single-crystal grains with helical chains (along a-axis) parallel to the substrate (**Figure S7d**). The final effective $\chi^{(2)}$ and $\chi^{(3)}$ in (R-MBA)Bi₄ polycrystalline film are related to the interactions between these oriented single-crystal grains with laser, so we study the polarized-

dependent SHG and THG of (R-MBA)BiI₄ single crystal to analyse the NLO response of the polycrystalline film.

The nonlinear polarization ($\mathbf{P}^{(2)}$ and $\mathbf{P}^{(3)}$) relate to the incident electric field \mathbf{E} and the nonlinear susceptibility tensor ($\chi_{ijk}^{(2)}$ and $\chi_{ijkl}^{(3)}$) as

$$P_i^{(2)} = \varepsilon_0 \sum_{jk} \chi_{ijk}^{(2)} E_j E_k \quad (1.1)$$

$$P_i^{(3)} = \varepsilon_0 \sum_{jkl} \chi_{ijkl}^{(3)} E_j E_k E_l \quad (1.2)$$

where i, j, k, l are the Cartesian indices. We consider an incident laser beam, $\mathbf{E} = |\mathbf{E}|(\cos(\delta)\mathbf{b} + \sin(\delta)\mathbf{c})\sin(\theta) + |\mathbf{E}|\cos(\theta)\mathbf{a}$, as shown in **Figure S8b**. Here, \mathbf{a} , \mathbf{b} , and \mathbf{c} are the crystallographic axes of (R-MBA)BiI₄. Since (R-MBA)BiI₄ belongs to the orthorhombic crystal system with 222 point group, its $\chi_{ijk}^{(2)}$ and $\chi_{ijkl}^{(3)}$ have 6 and 21 independent nonzero elements, respectively. We then expand Eqs. (1.1) and (1.2), respectively, to

$$\mathbf{P}^{(2)} = \frac{1}{2} \varepsilon_0 |\mathbf{E}|^2 ((\chi_{xyz}^{(2)} + \chi_{xzy}^{(2)}) \sin^2(\theta) \sin(2\delta)\mathbf{a} + (\chi_{yzx}^{(2)} + \chi_{yxz}^{(2)}) \sin(2\theta) \sin(\delta)\mathbf{b} + (\chi_{zxy}^{(2)} + \chi_{zyx}^{(2)}) \sin(2\theta) \cos(\delta)\mathbf{c}) \quad (1.3)$$

$$\begin{aligned} \mathbf{P}^{(3)} = & \varepsilon_0 |\mathbf{E}|^3 (\chi_{xxxx}^{(3)} \cos^3(\theta) + (\chi_{xxzz}^{(3)} + \chi_{xzxx}^{(3)} + \chi_{zzxx}^{(3)}) \cos(\theta) \sin^2(\theta) \sin^2(\delta) + (\chi_{xxyy}^{(3)} + \chi_{yyxy}^{(3)} + \chi_{xyyx}^{(3)}) \cos(\theta) \sin^2(\theta) \cos^2(\delta))\mathbf{a} \\ & + \varepsilon_0 |\mathbf{E}|^3 (\chi_{yyyy}^{(3)} \sin^3(\theta) \cos^3(\delta) + (\chi_{yyzz}^{(3)} + \chi_{zyyz}^{(3)} + \chi_{zyzy}^{(3)}) \sin^3(\theta) \cos(\delta) \sin^2(\delta) + (\chi_{yyxx}^{(3)} + \chi_{xyyx}^{(3)} + \chi_{yxyx}^{(3)}) \cos^2(\theta) \sin(\theta) \cos(\delta))\mathbf{b} \\ & + \varepsilon_0 |\mathbf{E}|^3 (\chi_{zzzz}^{(3)} \sin^3(\theta) \sin^3(\delta) + (\chi_{zzyy}^{(3)} + \chi_{zyzy}^{(3)} + \chi_{zyyz}^{(3)}) \sin^3(\theta) \cos^2(\delta) \sin(\delta) + (\chi_{zzxx}^{(3)} + \chi_{zxzx}^{(3)} + \chi_{zxxz}^{(3)}) \cos^2(\theta) \sin(\theta) \sin(\delta))\mathbf{c} \end{aligned} \quad (1.4)$$

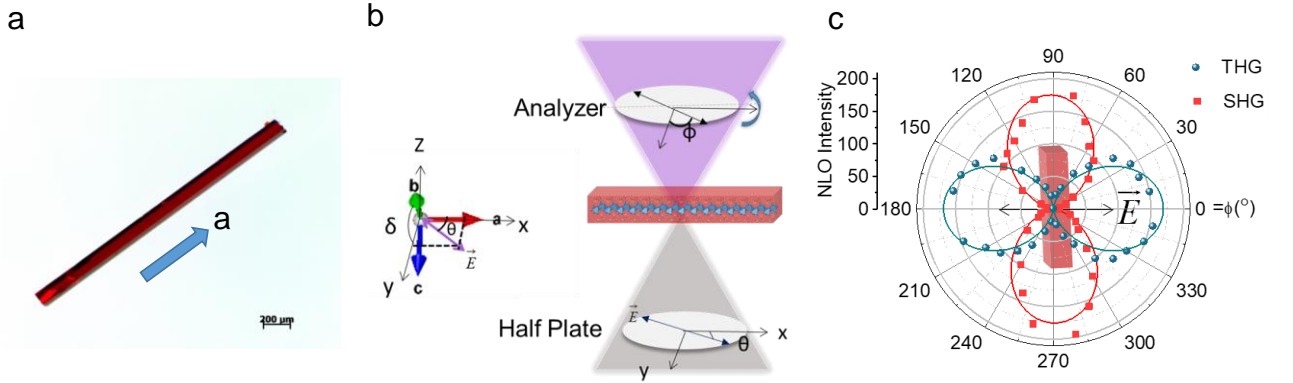


Figure S8. (a), Stereomicroscope picture of a (R-MBA)BiI₄ single crystal. \mathbf{a} represent the a-axis direction of (R-MBA)BiI₄ single crystal. (b), x, y, z directions are the experimental coordinates; \mathbf{a} , \mathbf{b} , \mathbf{c} are the crystallographic axes; the x-direction parallel to the a-axis. The pump laser is incident along the z-direction and polarized in x-y horizontal plane. δ is the angle between the b-axis and the y-direction; θ is the angle between the pump laser polarization and the a-axis; ϕ is the angle

between the axis of the analyser (linear polarizer) and the y-direction. (c), Polar plots of SHG and THG intensity of the (R-MBA)BiI₄ single crystal collected through rotating the analyser (angle ϕ) when the pumped laser is perpendicular to the a-axis of the (R-MBA)BiI₄ crystal (red cuboid). The dots represent the experimental data, and the solid curves indicate the theoretical fits by $I_2\cos^2(\phi-90^\circ)$ for SHG and $I_3\cos^2(\phi)$ for THG.

Let us consider two simple cases, i.e., $\theta=90^\circ$ and $\theta=0^\circ$. When $\theta=90^\circ$, that is, \mathbf{E} is polarized perpendicular to the a-axis of the (R-MBA)BiI₄ crystal, the Eqs. (1.3) and (1.4) become

$$\mathbf{P}^{(2)} = \frac{1}{2} \varepsilon_0 |\mathbf{E}|^2 (\chi_{xyz}^{(2)} + \chi_{xzy}^{(2)}) \sin(2\delta) \mathbf{a} \quad (1.5)$$

$$\begin{aligned} \mathbf{P}^{(3)} = & \varepsilon_0 |\mathbf{E}|^3 (\chi_{yyy}^{(3)} \cos^3(\delta) + (\chi_{yyz}^{(3)} + \chi_{yzy}^{(3)} + \chi_{zyz}^{(3)}) \cos(\delta) \sin^2(\delta)) \mathbf{b} \\ & + \varepsilon_0 |\mathbf{E}|^3 (\chi_{zzz}^{(3)} \sin^3(\delta) + (\chi_{zzy}^{(3)} + \chi_{zyz}^{(3)} + \chi_{zyz}^{(3)}) \cos^2(\delta) \sin(\delta)) \mathbf{c} \end{aligned} \quad (1.6)$$

In this case, the SHG signals generated are polarized along the a-axis and the THG signals are polarized in the b-c plane, as demonstrated in **Figure S8c**.

When $\theta=0^\circ$, that is, the pump light field \mathbf{E} is polarized parallel to the a-axis of the (R-MBA)BiI₄ crystal, the Eqs. (1.3) and (1.4) can be expressed as

$$\mathbf{P}^{(2)} = 0 \quad (1.7)$$

$$\mathbf{P}^{(3)} = \varepsilon_0 |\mathbf{E}|^3 \chi_{xxx}^{(3)} \mathbf{a} \quad (1.8)$$

In this case, the SHG signals vanish and the generated THG signals are polarized along a-axis.

For each grain (**Figure S7d**), \mathbf{E} can be decomposed into components in these two special directions (parallel to and perpendicular to the a-axis of single grain) based on θ . Then, the relationship between effective SHG and THG of (R-MBA)BiI₄ film and the single crystal grain orientations can be described by two parameters: θ (the angle between the pump laser polarization and the a-axis direction) and δ (crystal face). δ values are estimated to be $\sim 69^\circ$, $\sim 53^\circ$, and $\sim 79^\circ$ corresponding to (011), (012), and (021) faces, respectively. Due to the random distribution of θ for a large number of grains, we think the influence from grain orientations is nearly identical for different film samples.

Supplementary Note 2: Thickness-dependence of second- and third-harmonic generation in a lossy medium.

Considering our perovskite film contains no free charges, no free currents, and it is nonmagnetic, we can obtain the time-independent wave equation derived from Maxwell's equations at a frequency ω_n as follow¹³

$$\nabla^2 \mathbf{E}_n(\mathbf{r}) + \frac{\omega_n^2}{c^2} \tilde{\varepsilon}_n \mathbf{E}_n(\mathbf{r}) = -\frac{\omega_n^2}{\varepsilon_0 c^2} \mathbf{P}_n^{NL}(\mathbf{r}) \quad (2.1)$$

where $\mathbf{E}_n(\mathbf{r})$ represents electric field strength, $\mathbf{P}_n^{NL}(\mathbf{r})$ represents the nonlinear part of polarization field, and $\tilde{\varepsilon}_n$ is a complex dielectric tensor. In the above deduction, we assume $\nabla \cdot \mathbf{E}(\mathbf{r}, t) = 0$ for the slowly varying amplitude approximation in our thin film samples (at most several microns). $\mathbf{P}_n^{NL}(\mathbf{r})$ in Eq. 2.1 expand to

$$\mathbf{P}_n^{NL}(\mathbf{r}) = \varepsilon_o \chi^{(2)} \mathbf{E}_n(\mathbf{r}) \cdot \mathbf{E}_n(\mathbf{r}) + \varepsilon_o \chi^{(3)} \mathbf{E}_n(\mathbf{r}) \cdot \mathbf{E}_n(\mathbf{r}) \cdot \mathbf{E}_n(\mathbf{r}) + \varepsilon_o \chi^{(4)} \mathbf{E}_n(\mathbf{r}) \cdot \mathbf{E}_n(\mathbf{r}) \cdot \mathbf{E}_n(\mathbf{r}) \cdot \mathbf{E}_n(\mathbf{r}) + \dots \quad (2.2)$$

where the first item represents the second-harmonic generation, the second term represents the THG. In the following, we use subscript 1, 2, 3 to denote the corresponding quantities of the fundamental wave, SHG wave, and THG wave, respectively; we use an upper tilde ($\tilde{}$) to denote a quantity that is a complex; we use boldface to denote a quantity that is a vector.

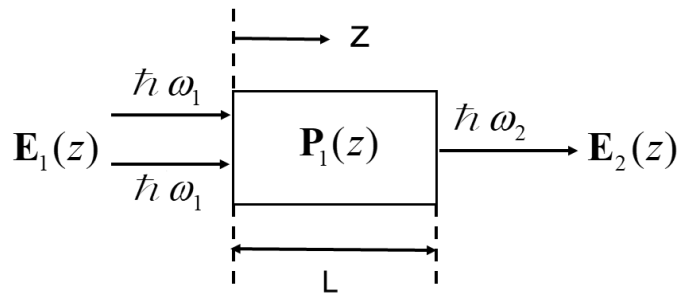


Figure S9. Second harmonic generation (SHG)

For SHG in a depleting medium, with pump wave propagating in the +z direction (namely normal to the substrate), $\mathbf{E}_1(\mathbf{r})$, $\mathbf{E}_2(\mathbf{r})$ and $\mathbf{P}_1^{NL}(\mathbf{r})$ can be expressed in scalar form as

$$E_1(z) = A_1(z)e^{i\tilde{k}_1 z} + c.c. = A_1(0)e^{i\tilde{k}_1 z} + c.c. \quad (2.4)$$

$$E_2(z) = A_2(z)e^{i\tilde{k}_2 z} + c.c. \quad (2.5)$$

$$P_1^{NL}(z) = \varepsilon_0 \chi_{\text{eff}}^{(2)} E_1(z)E_1(z) = \varepsilon_0 \chi_{\text{eff}}^{(2)} A_1(0)A_1(0)e^{i2\tilde{k}_1 z} + c.c. \quad (2.6)$$

where $\chi_{\text{eff}}^{(2)}$ represents the effective SHG susceptibility; $A(z)$ represent the wave amplitude; \tilde{k} is the complex wave vector, and $\tilde{k} = k + i\alpha/2$. Here, we assume no damping of the pump ω_1 wave, then, $A_1(z) = A_1(0)$, and $\tilde{k}_1 = k_1$. We now substitute Eqs. (2.4), (2.5) and (2.6) into the wave equation Eq. (2.1), and thereby obtain

$$\left(\frac{d^2 A_2(z)}{dz^2} + 2i\tilde{k}_2 \frac{dA_2(z)}{dz} - A_2(z)\tilde{k}_2^2 + \frac{\tilde{\varepsilon}_2 \omega_2^2}{c^2} A_2(z)\right)e^{i\tilde{k}_2 z} + c.c. = -\frac{\omega_2^2}{c^2} \chi_{\text{eff}}^{(2)} A_1(0)^2 e^{i2\tilde{k}_1 z} + c.c. \quad (2.7)$$

Since $\omega^2 \tilde{\varepsilon} = c^2(\tilde{k})^2$, the third and fourth terms on the left side of the equation cancel. The first term can be neglected when the SHG field amplitude is slowly varying along the z-direction,¹³ namely

$$\left|\frac{d^2 A_2(z)}{dz^2}\right| \ll \left|\tilde{k}_2 \frac{dA_2(z)}{dz}\right| \quad (2.8)$$

With this approximation, Eq. (2.7) becomes

$$\frac{dA_2(z)}{dz} = \frac{i\omega_2^2 \chi_{\text{eff}}^{(2)} A_1^2(0)e^{i(2\tilde{k}_1 - \tilde{k}_2)z}}{2\tilde{k}_2 c^2} \quad (2.9)$$

By integrating Eq. (2.9) from $z=0$ to $z=L$, the amplitude of the output SHG wave at the exit plane of the nonlinear medium is given as

$$A_2(L) = \frac{i\omega_2^2 \chi_{\text{eff}}^{(2)} A_1^2(0)}{2\tilde{k}_2 c^2} \int_0^L e^{i(2\tilde{k}_1 - \tilde{k}_2)z} dz = \frac{\omega_2^2 \chi_{\text{eff}}^{(2)} A_1^2(0)}{2\tilde{k}_2 c^2} \cdot \frac{e^{i(2\tilde{k}_1 - \tilde{k}_2)L} - 1}{(2\tilde{k}_1 - \tilde{k}_2)} \quad (2.10)$$

Here, we adopt the time-averaged Poynting vector (given by $I = 2\varepsilon_0 cn |\mathbf{E}|^2$) to calculate the intensity of the SHG wave as

$$I_2(L) = 2\varepsilon_0 cn_2 |\mathbf{E}_2(L)|^2 = 2\varepsilon_0 cn_2 |A_2(L)|^2 e^{-\alpha_2 L} = 2\varepsilon_0 cn_2 \frac{\omega_2^4 \chi_{\text{eff}}^{(2)2} A_1^4(0)}{|2\tilde{k}_2 c^2|^2} \left| \frac{e^{i(2\tilde{k}_1 - \tilde{k}_2)L} - 1}{(2\tilde{k}_1 - \tilde{k}_2)} \right|^2 e^{-\alpha_2 L} \quad (2.11)$$

$$I_1(L) = 2\varepsilon_0 cn_1 |\mathbf{E}_1(L)|^2 = 2\varepsilon_0 cn_1 |A_1(0)|^2 = I_1(0) \quad (2.12)$$

where $2\tilde{k}_1 - \tilde{k}_2 = 2k_1 - k_2 - i\alpha_2/2 = \Delta k^{(2)} - i\alpha_2/2$, $\tilde{k} = \frac{2\pi}{\lambda_0} \tilde{n}$, and $\tilde{n} = n + i\kappa$. $\Delta k^{(2)}$ is an important quantity usually called the wavevector mismatch. Finally, our expression for the SHG intensity can be obtained by introducing Eq. (2.12) into Eq. (2.11), yielding

$$I_2(L) = \frac{n_2 \omega_2^2}{8\varepsilon_0 n_1^2 c^3 |n_2|^2} \cdot \chi_{\text{eff}}^{(2)2} I_1(0)^2 \cdot \frac{(e^{-\alpha_2 L} - 2e^{-\alpha_2 L/2} \cos(\Delta k^{(2)} L) + 1)}{(\Delta k^{(2)})^2 + \alpha_2^2 / 4} e^{-\alpha_2 L} \quad (2.13)$$

In a similar derivation process, the expression for the THG intensity can be written as

$$I_3(L) = \frac{n_3 \omega_3^2}{16\varepsilon_0^2 n_1^3 c^4 |n_3|^2} \cdot \chi_{\text{eff}}^{(3)2} I_1(0)^3 \cdot \frac{(e^{-\alpha_3 L} - 2e^{-\alpha_3 L/2} \cos(\Delta k^{(3)} L) + 1)}{(\Delta k^{(3)})^2 + \alpha_3^2 / 4} e^{-\alpha_3 L} \quad (2.14)$$

Hence, the relation between SHG and THG intensity with film thickness (L) can be simplified as

$$I_2(L) \propto (e^{-\alpha_2 L} - 2e^{-\alpha_2 L/2} \cos(\Delta k^{(2)} L) + 1) \cdot e^{-\alpha_2 L} \quad (2.15)$$

$$I_3(L) \propto (e^{-\alpha_3 L} - 2e^{-\alpha_3 L/2} \cos(\Delta k^{(3)} L) + 1) \cdot e^{-\alpha_3 L} \quad (2.16)$$

where $\Delta k^{(2)} = 2k_1 - k_2 = \frac{2\pi}{\lambda_2}(n_1 - n_2)'$, $\Delta k^{(3)} = 3k_1 - k_3 = \frac{2\pi}{\lambda_3}(n_1 - n_3)'$, $\alpha_2 = \frac{4\pi\kappa_2}{\lambda_2}$, $\alpha_3 = \frac{4\pi\kappa_3}{\lambda_3}$, here, λ_2

and λ_3 are the SHG and THG wavelength in vacuum, respectively.

Table S5. The fitting Δk and α values for the dependence of the SHG and THG signals with the film thicknesses in **Figure 4b** based on Eqs. (2.15) and (2.16), compared with their experimental values calculated from n, κ (**Table S4**).

$\lambda_{\text{pump}} = 1200 \text{ nm}$	$\Delta k^{(2)} (\text{nm}^{-1})$	$\Delta k^{(3)} (\text{nm}^{-1})$	$\alpha_2 (\text{cm}^{-1})$	$\alpha_3 (\text{cm}^{-1})$
Fitting value	0.0027	0.0035	4.56×10^2	3.76×10^4
Experimental value	0.0027	0.0033	1.35×10^2	1.83×10^5

Supplementary Note 3: Quantification of the SHG and THG susceptibilities.

For simplicity, we can transform Eqs. (2.13) and (2.14) into the expressions of $\chi_{\text{eff}}^{(2)}$ and $\chi_{\text{eff}}^{(3)}$ as follow

$$\chi_{\text{eff}}^{(2)} = \left[\frac{I_2(L)}{I_1(0)^2} \frac{8\varepsilon_0 n_1^2 c^3 \left| \tilde{n}_2 \right|^2}{n_2 \omega_2^2} \frac{(\Delta k^{(2)})^2 + \alpha_2^2 / 4}{(e^{-\alpha_2 L} - 2e^{-\alpha_2 L/2} \cos(\Delta k^{(2)} L) + 1)} e^{\alpha_2 L} \right]^{1/2} \quad (3.1)$$

$$\chi_{\text{eff}}^{(3)} = \left[\frac{I_3(L)}{I_1(0)^3} \frac{16\varepsilon_0^2 n_1^3 c^4 \left| \tilde{n}_3 \right|^2}{n_3 \omega_3^2} \frac{(\Delta k^{(3)})^2 + \alpha_3^2 / 4}{(e^{-\alpha_3 L} - 2e^{-\alpha_3 L/2} \cos(\Delta k^{(3)} L) + 1)} e^{\alpha_3 L} \right]^{1/2} \quad (3.2)$$

Based on Eqs. (3.1) and (3.2), we can calculate the effective SHG and THG susceptibilities for (R-MBA)Bi₄ polycrystalline film at a pump wavelength of 1200 nm through equations below

$$\frac{\chi_{pe}^{(2)}}{\chi_{LNO}^{(2)}} = \left[\frac{(I_2 n_2 n_1^2 / \omega_2^2)_{pe}}{(I_2 n_2 n_1^2 / \omega_2^2)_{LNO}} \cdot \left(\frac{\Delta k^{(2)2} + \alpha_2^2 / 4}{e^{-\alpha_2 L} - 2e^{-\alpha_2 L/2} \cos(\Delta k^{(2)} L) + 1} e^{\alpha_2 L} \right)_{pe} \cdot \left(\frac{e^{-\alpha_2 L} - 2e^{-\alpha_2 L/2} \cos(\Delta k^{(2)} L) + 1}{\Delta k^{(2)2} + \alpha_2^2 / 4} e^{-\alpha_2 L} \right)_{LNO} \right]^{1/2} \quad (3.3)$$

$$\frac{\chi_{pe}^{(3)}}{\chi_{WS_2}^{(3)}} = \left[\frac{(I_3 n_3 n_1^3 / \omega_3^2)_{pe}}{(I_3 n_3 n_1^3 / \omega_3^2)_{WS_2}} \cdot \left(\frac{\Delta k^{(3)2} + \alpha_3^2 / 4}{e^{-\alpha_3 L} - 2e^{-\alpha_3 L/2} \cos(\Delta k^{(3)} L) + 1} e^{\alpha_3 L} \right)_{pe} \cdot \left(\frac{e^{-\alpha_3 L} - 2e^{-\alpha_3 L/2} \cos(\Delta k^{(3)} L) + 1}{\Delta k^{(3)2} + \alpha_3^2 / 4} e^{-\alpha_3 L} \right)_{WS_2} \right]^{1/2} \quad (3.4)$$

Here, the Pe, LNO and WS₂ subscripts represent physical quantities relating to ~600 nm (R-MBA)Bi₄ perovskite polycrystalline film, 600 nm X-cut LiNbO₃ single-crystal film, and monolayer WS₂, respectively. For X-cut LiNbO₃ single crystal film, the incident polarization of the pump beam was along its z-axis, and the SHG radiation along its z-axis was collected, leading to a known SHG susceptibility χ_{33} ($\chi_{33} = 2d_{33}$). The corresponding results are presented in **Table S6**.

Table S6. The film thickness L , refractive index n , absorption coefficient α , nonlinear response intensity I and $\chi^{(2)}$ and $\chi^{(3)}$ values for (R-MBA)Bi₄, LiNbO₃, and WS₂. Here, subscripts 1, 2, and 3

represent the parameters at a pump wavelength of 1200 nm, SHG wavelength of 600 nm, and THG wavelength of 400 nm, respectively. The units of pump wavelength (λ_{pump}), α , $\chi^{(2)}$, and $\chi^{(3)}$ are nm, cm^{-1} , pm V^{-1} , and $\text{pm}^2 \text{V}^{-2}$, respectively. The n , κ value of LiNO_3 ¹⁴ and WS_2 ¹⁵, the $\chi^{(2)}$ of LiNO_3 ,¹⁶ and the $\chi^{(3)}$ of WS_2 ¹⁷ are taken from references.

	L	n_1	n_2	n_3	α_2	α_3	I_2	I_3	$\chi_{\text{eff}}^{(2)}$	$\chi_{\text{eff}}^{(3)}$
Pe	600	1.79	2.06	2.00	1.35×10^2	1.83×10^5	37854	3571	$0.47 \times L$	$35.33 \times$
								1	NO	WS_2
LNO	600	2.22	2.29	2.44	~ 0	~ 0	12622	/	83.40	/
							0	/		
WS_2	0.70	2.81	2.63	3.22	3.19×10^5	8.56×10^5	/	58	/	2.40×10
										5

From the wavelength-dependent spectra, we know that the strong exciton resonance is not located at 1200 nm, but around 1550 nm (an important communication band), so we calculated the enhanced SHG and THG susceptibilities for (R-MBA)BiI₄ polycrystalline film at 1550 nm compared with the above results at 1200 nm through equations below

$$\frac{\chi_{1550}^{(2)}}{\chi_{1200}^{(2)}} = \left[\frac{(I_2 n_2 n_1^2 / \omega_2^2)_{1550}}{(I_2 n_2 n_1^2 / \omega_2^2)_{1200}} \cdot \left(\frac{\Delta k^{(2)2} + \alpha_2^2 / 4}{e^{-\alpha_2 L} - 2e^{-\alpha_2 L/2} \cos(\Delta k^{(2)} L) + 1} e^{\alpha_2 L} \right)_{1550} \cdot \left(\frac{e^{-\alpha_2 L} - 2e^{-\alpha_2 L/2} \cos(\Delta k^{(2)} L) + 1}{\Delta k^{(2)2} + \alpha_2^2 / 4} e^{-\alpha_2 L} \right)_{1200} \right]^{1/2} \quad (3.5)$$

$$\frac{\chi_{1550}^{(3)}}{\chi_{1200}^{(3)}} = \left[\frac{(I_3 n_3 n_1^3 / \omega_3^2)_{1550}}{(I_3 n_3 n_1^3 / \omega_3^2)_{1200}} \cdot \left(\frac{\Delta k^{(3)2} + \alpha_3^2 / 4}{e^{-\alpha_3 L} - 2e^{-\alpha_3 L/2} \cos(\Delta k^{(3)} L) + 1} e^{\alpha_3 L} \right)_{1550} \cdot \left(\frac{e^{-\alpha_3 L} - 2e^{-\alpha_3 L/2} \cos(\Delta k^{(3)} L) + 1}{\Delta k^{(3)2} + \alpha_3^2 / 4} e^{-\alpha_3 L} \right)_{1200} \right]^{1/2} \quad (3.6)$$

Here, the 1200 and 1550 subscript represent physical quantities relating to (R-MBA)BiI₄ perovskite film at $\lambda_{\text{pump}}=1200$ nm and $\lambda_{\text{pump}}=1550$ nm, respectively. The corresponding results are presented in **Table S7**.

Table S7. The n , α and I values for (R-MBA)BiI₄ with a film thickness of 145 nm. The units of λ_1 , α , $\chi^{(2)}$, and $\chi^{(3)}$ are nm, cm⁻¹, pm V⁻¹, pm² V⁻², respectively.

	λ_1	n_1	n_2	n_3	α_2	α_3	I_2	I_3	$\chi_{eff}^{(2)}$	$\chi_{eff}^{(3)}$
P	1200	1.79	2.06	2.00	1.35×10^2	1.83×10^5	2875	15609	39.4	8.48×10^6
e	1550	1.75	1.90	2.02	10.5	1.03×10^5	21932	69414	130. 5	8.99×10^6

Supplementary References

- (1) Sheldrick, G. M., SHELXT - integrated space-group and crystal-structure determination. *Acta Crystallogr. A Found. Adv.* **2015**, *71*, 3-8.
- (2) Sheldrick, G. M., Crystal structure refinement with SHELXL. *Acta Crystallogr. C Struct. Chem.* **2015**, *71*, 3-8.
- (3) Sheldrick, G. M., A short history of SHELX. *Acta Crystallogr. A* **2008**, *64*, 112-22.
- (4) Dolomanov, O. V.; Bourhis, L. J.; Gildea, R. J.; Howard, J. A. K.; Puschmann, H., OLEX2: a complete structure solution, refinement and analysis program. *J. Appl. Crystallogr.* **2009**, *42*, 339-341.
- (5) Momma, K.; Izumi, F., VESTA 3 for three-dimensional visualization of crystal, volumetric and morphology data. *J. Appl. Crystallogr.* **2011**, *44*, 1272-1276.
- (6) Gu, H.; Chen, X.; Jiang, H.; Zhang, C.; Liu, S., Optimal broadband Mueller matrix ellipsometer using multi-waveplates with flexibly oriented axes. *J. Opt.* **2016**, *18*, 025702.
- (7) Kresse, G.; Furthmüller, J., Efficiency of ab-initio total energy calculations for metals and semiconductors using a plane-wave basis set. *Comput. Mater. Sci.* **1996**, *6*, 15-50.
- (8) Kresse, G.; Furthmüller, J., Efficient iterative schemes for ab initio total-energy calculations using a plane-wave basis set. *Phys. Rev. B* **1996**, *54*, 11169-11186.
- (9) Blochl, P. E., Projector augmented-wave method. *Phys. Rev. B* **1994**, *50*, 17953-17979.
- (10) Kresse, G.; Joubert, D., From ultrasoft pseudopotentials to the projector augmented-wave method. *Phys. Rev. B* **1999**, *59*, 1758-1775.
- (11) Perdew, J. P.; Burke, K.; Ernzerhof, M., Generalized Gradient Approximation Made Simple. *Phys. Rev. Lett.* **1996**, *77*, 3865-3868.

- (12) Shi, W.; Lin, M.-L.; Tan, Q.-H.; Qiao, X.-F.; Zhang, J.; Tan, P.-H., Raman and photoluminescence spectra of two-dimensional nanocrystallites of monolayer WS₂ and WSe₂. *2D Mater.* **2016**, *3*, 025016.
- (13) Boyd, R. W., *Nonlinear Optics*. Academic Press: 2008.
- (14) Zelmon, D. E.; Small, D. L.; Jundt, D., Infrared corrected Sellmeier coefficients for congruently grown lithium niobate and 5 mol% magnesium oxide -doped lithium niobate. *J. Opt. Soc. Am. B* **1997**, *14*, 3319.
- (15) Ermolaev, G. A.; Yakubovsky, D. I.; Stebunov, Y. V.; Arsenin, A. V.; Volkov, V. S., Spectral ellipsometry of monolayer transition metal dichalcogenides: Analysis of excitonic peaks in dispersion. *J. Vac. Sci. Technol. B* **2020**, *38*, 014002.
- (16) Boyd, G. D.; Miller, R. C.; Nassau, K.; Bond, W. L.; Savage, A., LiNbO₃: an efficient phase matchable nonlinear optical material. *Appl. Phys. Lett.* **1964**, *5*, 234-236.
- (17) Autere, A.; Jussila, H.; Marini, A.; Saavedra, J. R. M.; Dai, Y.; Säynätjoki, A.; Karvonen, L.; Yang, H.; Amirsolaimani, B.; Norwood, R. A.; Peyghambarian, N.; Lipsanen, H.; Kieu, K.; de Abajo, F. J. G.; Sun, Z., Optical harmonic generation in monolayer group-VI transition metal dichalcogenides. *Phys. Rev. B* **2018**, *98*, 115426.